

**THE OPERATIONAL CMC/ MRB
GLOBAL ENVIRONMENTAL MULTISCALE (GEM) MODEL**

Jean Côté ^{*}, Jean-Guy Desmarais [#], Sylvie Gravel ^{*}, André Méthot [#],
Alain Patoine [#], Michel Roch ^{*} and Andrew Staniforth ^{*}

^{*} Recherche en prévision numérique

[#] Canadian Meteorological Centre

Service de l'environnement atmosphérique

2121 Route Transcanadienne, porte 500

Dorval, Québec

CANADA H9P 1J3

1. INTRODUCTION

Environment Canada is tasked with providing both existing and new atmospheric environmental services to the Canadian public and to policy makers. To address present and anticipated needs, an innovative and integrated atmospheric environmental forecasting and simulation system, described herein, is being developed by the Meteorological Research Branch (MRB) in partnership with the Canadian Meteorological Centre (CMC). The bilingual acronym **GEM** has been adopted for the model around which this system is constructed. Thus in English the model is designated as "the **Global Environmental Multiscale** model", whereas in French it is referred to as "le modèle **Global Environnemental Multi-échelle**".

There are three important motivations for modeling the atmosphere. These are to: forecast the weather; address climate issues such as global change; and address air quality issues such as smog, ozone depletion, and acid rain. Since the atmosphere is a relatively shallow layer (one to two orders of magnitude smaller than the Earth's radius) of fluid surrounding a rotating sphere it can be modeled, to leading order and in the absence of sources and sinks of otherwise conserved quantities (e.g. mass, momentum and energy), using the classical fluid dynamic equations for rotating fluids. To these are appended transport equations for various atmospheric tracers such as cloud liquid water and chemical species such as ozone, hydrocarbons and aerosols. A comprehensive air-quality model may have hundreds of such chemical species.

To close the mathematical description of the physical and chemical problems, the various source, sink and redistribution forcing terms of the governing equations must be prescribed or (more usually) parameterized. These for the most part are associated with phenomena that are either not described by the fluid dynamic equations or, if described, that are not explicitly resolved because they occur at the sub-grid scale of a necessarily-finite mesh. Parameterizations can be (and usually are) complex models in their own right. Examples of unrepresented or unresolved phenomena include: turbulent fluxes of momentum, heat and moisture over land, water, and ice;

solar and infrared radiation; clouds and cloud processes; precipitation; and chemical reactions. The phenomena that appear as forcing terms generally mutually interact in a nonlinear manner.

A numerical model of the atmosphere can be considered to be an integrating tool that permits various sub-systems to mutually interact via the nonlinear forcing terms of the coupled set of equations. The potential atmospheric phenomena to be modeled cover a very-broad range of time and space scales. Temporally they vary from the sub-second scales of some chemical reactions to the hours, days, weeks, and perhaps months, of weather forecasting, to the years, decades, centuries and millenia of climate simulation. Spatially they vary from the fractions of a meter of chemical reactions and molecular diffusion, right through to the global scale of tens of thousands of kilometers. For the results to be meaningful and useful, numerical models must be run with time and space scales that are commensurate with those associated with the phenomena of interest, and this of course imposes serious practical constraints and compromises.

Assimilation (see e.g. Daley 1991 for a review) of both in-situ data (e.g. from radiosondes) and remotely-sensed data (e.g. from satellite-mounted instruments), provides both the initial conditions (i.e. analyses) required for numerical weather prediction and a means of monitoring climate change. It can also provide initial conditions for chemical species, such as ozone. The development of sophisticated (and computationally expensive) assimilation methods is an area of intense research at the present time. These include three- and four-dimensional variational assimilation and extended Kalman filtering. Since numerical models of the atmosphere are usually used as constraints for data assimilation, present and anticipated developments in data assimilation must be taken into account when designing new numerical models of the atmosphere.

The goals of the present paper are to:

- motivate and outline the staged and ongoing development of a comprehensive and fully-integrated global atmospheric environmental forecasting and simulation system;
- discuss various design considerations;
- summarize the current status of development; and

- present proof-of-concept results for the key and pivotal component of the system, a global variable-resolution atmospheric model (GEM), that have led to its recent operational implementation at the CMC for regional weather forecasting.

The emphasis here is on the concepts underlying the long-term developmental strategy, and on results obtained using the described GEM model at its present state of development, rather than on a detailed description of its numerics since this is expected to further evolve.

The anticipated readership of this document is very broad. It includes operational forecasters, principally at regional offices across Canada but also some in foreign weather forecasting services; R&D personnel both within Environment Canada and abroad; and university professors both within Canada and abroad. Because of the diverse interests of such a diverse readership some compromises must necessarily be made when writing an article such as this. We could have limited both the content and interest of this article to some subset of the readership, but we have chosen not to do so. We have chosen instead to provide more comprehensive information in a fairly modular way, and to invite readers to skim over or ignore the sections that do not particularly interest them, and to concentrate on those that do. In this way we hope all readers will find something here of interest and use to them.

2. RATIONALE FOR THE DEVELOPMENT OF A UNIVERSAL MODEL

a. Operational weather forecasting considerations

Two operational data assimilation and weather forecasting cycles, one global and one regional, have been running daily at the Canadian Meteorological Centre for a number of years: a similar strategy is also employed at a majority of the larger operational numerical-weather-prediction centers. The global cycle addresses medium-range forecasting needs (i.e. forecasting for periods greater than two days) by using a global data-assimilation system (Mitchell et al. 1996) and the SEF model, a uniform-resolution global spectral forecast model (Ritchie and Beaudoin 1994). Spectral here refers to the use of an expansion of the dependent variables in terms of the spectral functions of the Laplace operator on the sphere, viz. spherical harmonics, in the context of

a Galerkin method. The current configuration of the SEF model is T199L21, i.e. the spherical harmonic series is triangularly truncated at wavenumber 199 and there are 21 levels in the vertical with the top level at $\sigma = 0.01$. Here $\sigma \equiv p/p_s$ is the terrain-following vertical coordinate, p is pressure, and p_s is its value at the Earth's surface.

The global cycle, until very recently, also initialized the 12-h regional data-assimilation spin-up system (Chouinard et al. 1994) of the second (regional) cycle. This latter provided the higher-resolution regional analyses used by the variable-resolution regional finite-element (RFE) model (Mailhot et al. 1997) to produce more-detailed short-range (< 2 days) forecasts over N. America and some of its adjacent waters. The RFE model focuses resolution over an area of interest, and the horizontal mesh used operationally until its recent replacement by the new global variable-resolution (GEM) model described herein, is displayed in [Fig. 1](#). This mesh is defined on a polar-sterographic projection, true at 60° N. Over the N. American area of interest, it has uniform 35-km resolution, and the resolution smoothly degrades outwards away from this uniform-resolution sub-domain: moving outwards, each successive meshlength is approximately 10% larger than its preceding neighbour. The RFE model has the same vertical coordinate system as the global spectral model, but it was operationally configured to have 28 levels instead of 21.

The described two-cycle strategy requires the maintenance, improvement and optimization of two sets of libraries and procedures. This is very labor intensive, principally for three reasons. First, numerical weather prediction models need significant recoding in order to reap the benefits afforded by the new high-performance significantly-parallel computer platforms. Second, to improve the accuracy of the initial state of the atmosphere, i.e. that of the analysis, requires a significant investment in the research and development of new data assimilation methods. In this regard, the development of the tangent linear model of a forecast model and its adjoint, needed for four-dimensional data assimilation (see e.g. Courtier et al. 1994), is quite costly. Third, to improve the predictive capability of a weather forecast model requires a significant effort to be devoted to the improvement of model parameterizations. These considerations therefore motivate

the consolidation of both the global and regional assimilation and forecasting systems within a single flexible model framework, thereby rationalizing human resource utilization.

b. Air quality modeling considerations

It is advantageous to also embed within this proposed model a module for the transport and conversion of chemical species in order to address a wide range of air-quality issues. In this way, and as noted in the research study of Dastoor & Pudykiewicz (1996), the physical processes in the atmosphere, advection, and chemical conversions, are all computed within the framework of a consistent modeling system. Furthermore, this approach has the additional benefit of permitting the assimilation of observations of chemical species such as ozone in a self-consistent manner, and of using adjoint methods for establishing source-receptor relations.

Having such a modeling capability for chemical species is not only beneficial for research and policy-advice purposes but also for operational applications. In the event of an environmental emergency the CMC is responsible for running an environmental-emergency-response (EER) model (D'Amours et al. 1995), and providing information and guidance to the authorities to help them best respond to the situation. Examples of environmental emergencies include: the release of airborne toxic chemicals such as nuclear material (see e.g. Pudykiewicz 1989), with the pressing need to apply mitigation measures or even evacuate the population from downstream areas; and the eruption of volcanos (see e.g. Heffter and Stunder 1993), with the need to warn aircraft of ash plume location in order to avoid catastrophic engine failure and subsequent loss of life and aircraft. CMC's current operational EER model is based on the off-line transport and chemical conversion model described in Pudykiewicz (1989). Embedding this off-line model in the GEM model at the heart of the above-motivated flexible modeling system would potentially, for example, not only permit improvement of the operational procedures for analysing and forecasting ozone and the UV-B index, but also more accurate weather forecasts due to an improved radiation budget based on a reliable ozone distribution.

c. Non-hydrostatic mesoscale modeling considerations

The Canadian mesoscale community needs a non-hydrostatic mesoscale research model to be available for the development and validation of physical parameterizations, such as moist convection, gravity-wave drag, and surface- and boundary- layer phenomena, and also for nowcasting research. This need is presently fulfilled by the MC2 (Mesoscale Compressible Community) model (Benoit et al. 1997). It uses the fully-compressible Euler equations rather than the hydrostatic primitive equations, the subset of these equations traditionally used for operational weather forecasting. Such a model can be used for atmospheric flows having horizontal scales of motion considerably smaller than the 10 km or so scale limitation imposed by the hydrostatic assumption of the hydrostatic primitive equations.

By using the fully-compressible Euler equations in the context of the proposed single universal model strategy, the described need for a non-hydrostatic mesoscale research model could be easily met. This would result in a further significant rationalization of resources.

d. Climate modeling considerations

While it is not presently a project priority, it would be possible to use the proposed global environmental multiscale modeling framework for climate modeling applications such as global-warming scenarios and regional climate applications (Déqué and Piedelievre 1995; Fox-Rabinowitz et al. 1997).

As time progresses, the distinction between weather forecast and climate models becomes ever blurred due to the increased sophistication of parameterizations in weather forecast models and the increased resolution of climate models. Evidence for this is provided by the diverse mix of weather forecasting and climate models used by participants to make 10-year simulations in the Atmospheric Model Intercomparison Project (Gates 1992, 1995). It is now possible to configure a global atmospheric circulation model for either weather forecasting or climate applications simply by fixing the resolution and choosing between available parameterizations. The advantages of doing this within a single universal model framework is threefold. First, it is more economical in

terms of human resources since there is only one modeling infrastructure to be maintained, improved and optimized. Second, any improvements (e.g. better parameterizations, numerical algorithms, diagnostics, optimized code etc.) developed for weather forecasting or for climate simulation, are immediately available for other applications without having to spend scarce, and possibly unavailable, resources on code transplantation and validation. Third, improved validation of parameterizations is possible because they can be easily tested for both weather forecasting and climate applications - good parameterizations should be expected to lead to both accurate weather forecasts and realistic climate simulations.

e. In summary

The foregoing motivates the development of a new highly-flexible modeling system capable of meeting the weather-forecasting needs, both operational and research, of Canada for the coming years. Such a modeling system also has the potential to meet the air quality and climate modeling needs. A discussion follows of some of the more important design considerations for the universal GEM model at the heart of this flexible modeling system.

3. VARIABLE HORIZONTAL RESOLUTION

a. Rationale for global variable resolution

The principal objective of numerical weather prediction is to make a high-resolution forecast over the largest-possible area having the longest-possible time period of validity. This involves two conflicting goals: high resolution, and validity for large areas and long time periods. The compromise of regional modeling is to favour high resolution at the expense of reduced domain size and period of validity. As discussed in Staniforth (1997), strategies for regional modeling fall into two broad classes: interactive and non-interactive.

The principal difficulty with the *non-interactive* approach is the specification of the correct number and type of lateral boundary conditions for open domains, and this is related to fundamental problems of mathematical well-posedness (Olinger and Sundström 1978). In the *interactive* approach, the resolution is varied in some manner away from the fine resolution of an

area of interest to the coarser resolution of a surrounding outer region. It has the desirable features that the flows inside and outside the area of interest mutually interact in a single dynamic system, and that it also addresses the well-posedness issue of limited-area models at the cost of integrating over a larger domain. A smooth degradation of the resolution outside the area of interest can reduce this cost, and this also avoids the deleterious impact on the accuracy of the solution, discussed in Gravel and Staniforth (1992), of an abrupt change in resolution.

The domain of the surrounding outer region of an interactive-strategy model is usually taken to be either quasi-hemispheric or global. Imposing a wall boundary condition in the equatorial region, as in e.g. the formerly-operational CMC Regional Finite Element model (Mailhot et al. 1997) and the operational U.S. Nested Grid Model (DiMego et al. 1992), has the virtue of yielding a well-posed problem but, to be consistent, does require modification of the initial conditions. Taking the domain to be *global*, as advocated here, is less restrictive.

b. Different approaches to global variable-resolution

The key element to attain the stated goals is the adoption of *variable resolution* for the horizontal discretization. Variable resolution over the globe can be achieved in a number of different ways. In Courtier and Geleyn (1988) and Hardiker (1997) a continuous coordinate mapping due to Schmidt (1977) is employed such that the efficiency of the spectral method is hardly affected, and this approach is used in Météo France's operational ARPEGE model (Courtier et al. 1991). However the nature of the conformal coordinate transformation limits the focusing of the resolution to, roughly-speaking, meso-beta-scale applications (Caian and Geleyn 1997). A different continuous coordinate mapping, which is weakly-varying and orthogonal but non-conformal, is used in Sharma et al. (1987) in the context of a finite-difference discretization. In Paegle (1989), Paegle et al. (1997) and Côté et al. (1993), variable resolution is achieved using finite elements. For the Paegle et al. (1989, 1997) formulation the resolution is varied and focused in the North-South coordinate direction only.

The Côté et al. (1993) formulation adopted here is more general, and it permits resolution to be simultaneously varied in both coordinate directions in a flexible manner. It is an adaptation of the variable-resolution approach of the RFE model to spherical geometry using a regular (but variable-resolution) arbitrarily-rotated lat-lon mesh. A regular lat-lon mesh facilitates computational efficiency since its regularity is reflected in the resulting matrix structures, and certain properties that only hold for regular meshes can then be exploited (see Staniforth 1987 for discussion). Rotating the mesh permits resolution to be focused not only over mid-latitudinal areas of interest, but also tropical ones, thus addressing the above-mentioned limitation of the RFE model. Motivated by regional climate modeling considerations, Fox-Rabinowitz et al. (1997) also use the variable-resolution strategy advocated here.

c. Different mesh configurations for different applications

For *global-scale* problems, such as medium-range, monthly, and seasonal weather forecasting, the long-range transport of pollutants, and climate scenarios, a *uniform* lat-lon mesh configuration is appropriate; configured this way the GEM model can replace the global spectral model.

For smaller-scale problems, several variable-resolution horizontal mesh configurations are displayed in Figs. 2-4, illustrating the flexibility of the approach. The first of these, shown from two different viewing perspectives in Figs. 2a-b, is suitable for forecasting at the *continental* scale for periods of up to 48 h. Over N. America the resolution is 0.33° , and the resolution smoothly degrades away from the uniform-resolution subdomain in the same manner as for the RFE model: each successive mesh-length is approximately 10% larger than that of its preceding neighbour. This mesh both covers approximately the same area and has approximately the same resolution as that of the formerly-operational RFE model (cf. Figs. 1 and 2). It also, perhaps surprisingly, has 5% fewer degrees of freedom: this is because it is more efficient to work directly on the globe rather than on a distorted projection of it. The GEM model is operationally configured by the CMC to use the grid configuration of Fig. 2 to provide regional forecasts to 48 h. The

uniformly (in latitude and longitude) spaced meshpoints of the high-resolution window are also almost uniformly spaced over the sphere with meshlengths that vary between a maximum of approximately 37 km (for meshlengths oriented West to East) and a minimum of 29 km (attained on the Atlantic and Pacific boundaries). This may be compared to the high-resolution window of the formerly-operational RFE mesh, where the corresponding meshlength spacing over the sphere varies from approximately 38 km (near the N. Pole) to 25 km (in the Caribbean). Although this is not an essential element of the strategy, it was found convenient to orient the mesh as in Fig. 2. This is because it gives somewhat enhanced resolution at inflow on the western geographical boundary of the high-resolution window, and because it also gives a vector length of 255 which is well-suited to the architecture of the NEC SX-4 computer.

The second grid configuration (Fig. 3) is suitable for *provincial*-scale problems, such as forecasting the weather in more detail for periods up to perhaps 12 h. The resolution is now focused over a much smaller-size ($10^\circ \times 10^\circ \sim 1100 \text{ km} \times 1100 \text{ km}$) uniform-resolution sub-domain, which is centered over British Columbia for this example. The resolution ($0.033^\circ \sim 3.6 \text{ km}$) of this sub-domain is ten times finer than that of Fig. 2. The third grid configuration (Fig. 4) is suitable for *urban*-scale problems, such as simulating an urban smog episode for a few hours, and the mesh is now centered over Montreal island. For this highly-focused mesh, the resolution ($0.0033^\circ \sim 360 \text{ m}$) is further increased by a factor of ten and focused over a fifty-times-smaller ($1.36^\circ \times 1.36^\circ \sim 150 \text{ km} \times 150 \text{ km}$) sub-domain. For both the *provincial*- and *urban*-scale meshes (Figs. 3-4), the resolution again varies smoothly away from the uniform-resolution sub-domain, with the same approximately 10% successive increase in meshlength as for the *continental*-scale configuration (Fig. 2).

d. Mesh properties

All three of the shown mesh configurations have the remarkable property that *at least 50% of the total meshpoints* (i.e. at least 70% for each of the two coordinate directions) *are over the uniform high-resolution area of interest*. This implies that the overhead of using a variable-

resolution global model for very-small-scale applications over small areas is small indeed, and compares well to that associated with the surrounding sponge regions of traditional open-boundary limited-area models.

This particular variable-resolution strategy has the property that it becomes increasingly cost-effective as a function of increasing resolution for an area of interest of fixed size. To see this, consider the cost of increasing the resolution over the uniform-resolution subdomain of [Fig. 2](#) while holding its size fixed, and while also smoothly degrading the resolution away from this subdomain in exactly the same manner: i.e. each successive meshlength is always approximately 10% larger than its predecessor when moving outwards in any of the four compass directions. The percentage of points over the uniform-resolution N. American subdomain then increases exponentially (see [Fig. 5](#), obtained using the analysis given in Appendix A) as a function of increasing resolution over the subdomain. For example, at the 0.33° resolution of [Fig. 2](#), 57% of the total number of meshpoints are over the (fixed-size) uniform-resolution subdomain, whereas the percentage at 0.25° and 0.1° of resolution respectively increases to 63% and 78%. When sufficient computer power becomes available for the CMC to operationally increase the resolution of the regional configuration of the new model to 10 km (the estimated limit on resolution of a hydrostatic model), the percentage of meshpoints over the uniform-resolution subdomain will go from today's 57% (approximately 76% in each of the two horizontal directions) to 78% (approximately 88% in each of the two horizontal directions). This clearly illustrates the point that this global variable-resolution strategy, which is already highly competitive with driven limited-area models such as the MC2 model, will become ever more so in the future. It also has the clear advantage that it does not suffer from ill-posedness problems at lateral boundaries, nor difficulties associated with abrupt jumps in resolution across them.

4. OTHER NUMERICAL MODELING DESIGN CONSIDERATIONS

a. Non-hydrostatic considerations

The hydrostatic assumption, viz. the neglect of vertical acceleration in the vertical momentum equation, is an excellent approximation that is well respected in the atmosphere down to scales of 10 km or so. However at these scales the non-hydrostatic effects excluded by the hydrostatic assumption start to become non-negligible, for example internal wave breaking and overturning. To date, computer limitations have been such that operational weather-forecast (and climate-simulation) models have been run with horizontal meshlengths coarse enough to confidently employ the hydrostatic primitive equations. Looking to the future however, this will change. In particular, if the new model is to be applied over the provincial and urban mesh configurations of [Figs. 3-4](#), then it should use the fully-compressible Euler equations instead of the so-called hydrostatic primitive ones. This motivates the use of the "hydrostatic-pressure" vertical coordinate proposed in Laprise (1992). This coordinate system permits a switch-controlled choice between the hydrostatic primitive equations (for large- and synoptic-scale applications), and the non-hydrostatic Euler equations (for smaller-scale applications), thus getting the best of two worlds. A terrain-following normalized pressure (Phillips 1957; Kasahara 1974) version is possible. It allows easy incorporation of the lower boundary such that the coordinate surfaces relax towards the horizontal upwards from the Earth's surface. This terrain-following "hydrostatic-pressure" coordinate reverts to the usual hybrid coordinate of hydrostatic primitive equation models when the switch is set to the hydrostatic option. The resulting coordinate system has the advantage that it permits a straightforward adaptation of an existing library of physical parameterizations developed over the last decade or so. Although the new model has been formulated in terms of this terrain-following "hydrostatic-pressure" coordinate, at the present state of development the code only exists for the hydrostatic primitive equations. The development of the fully-compressible Euler equations option is however in progress.

b. Efficient time integration schemes

Numerical efficiency is of prime importance when modeling the atmosphere. There are basically three types of signal speed in the atmosphere: acoustic, gravity, and local wind. The acoustic waves carry negligible energy and propagate the fastest. The gravity waves carry relatively little energy, particularly at large scales, and propagate somewhat slower, but the fastest of these (termed the external modes) still propagate much faster than the local windspeed. The timestep of explicit Eulerian integration schemes is restricted by the fastest signal speed, which means that in the atmosphere the timestep is constrained by the modes which carry the least energy. This motivates the use of an *implicit time treatment of the terms that govern the propagation of the acoustic and gravitational oscillations*.

For an Eulerian treatment of advection, such an approach results in the timestep then being limited by the usual local Courant number ($U \Delta t / \Delta x$) being constrained to be somewhat less than unity. For a lat-lon representation of the sphere this is particularly restrictive in polar regions due to the convergence of the meridians, but elsewhere it still restricts the timestep to be several factors smaller than that dictated by the spatial truncation error. In other words, the timestep can still be significantly lengthened without loss of accuracy provided a more stable treatment of advection is adopted. This motivates the use of a *semi-Lagrangian treatment of advection* (Robert 1981, 1982; see Staniforth and Côté 1991 for a review), which is stable for Courant numbers much greater than unity. The governing equations are thus approximated along a parcel trajectory that arrives at a meshpoint at the new timestep. The evaluation of substantive derivatives then reduces to taking a time difference along a trajectory. Upstream values are computed by interpolation (usually cubic) of values at meshpoints surrounding the departure point (which is generally not a meshpoint). Semi-implicit semi-Lagrangian methods were originally developed for hydrostatic primitive equation models. They have since been extended to the fully-compressible Euler equations (Tanguay et al. 1990; Semazzi et al. 1995).

c. Monotonicity and conservation

The interpolation procedure can give rise to a local violation of monotonicity (due to the Gibbs phenomenon), and this motivates adoption of the monotonic scheme of Bermejo and Staniforth (1992). In this scheme a high-order estimate (using cubic interpolation) is blended with a low-order one (using linear interpolation which guarantees monotonicity). Consistent with approximation theory, the blending is done in such a way that the high-order solution is favoured whenever smoothness warrants it (i.e. most of the time), otherwise the low-order solution is more strongly weighted. This algorithm is of particular importance for the transport of physical and chemical species since the parameterized processes often assume that the transported quantities are non-negative on physical grounds, and it is used in the operational regional configuration of the new model.

The conservation of physical and chemical species, while excellent, is not exact. Priestley (1993) introduced a conserving variant of the monotonic Bermejo and Staniforth (1992) algorithm such that conservation is additionally enforced as a constraint via a minimization procedure, with adjustments being made where most warranted. This option is however not as yet available at the current state of development.

d. Tangent linear model and its adjoint

An intense effort is being made internationally to develop powerful four-dimensional data assimilation methods to improve the accuracy of the approximate representation of the initial state of the atmosphere. The more promising of these methods require the tangent linear model, and its adjoint, of the underlying atmospheric model to be available.

5. PROJECT HISTORIC

a. Shallow-water equations prototype

A two-dimensional shallow-water prototype (Côté et al. 1993) was developed to provide the "proof-of-concept" for the horizontal variable-resolution strategy. The numerical discretization has subsequently evolved and the shallow-water model has been tested extensively on meshes such as those of [Figs. 2-4](#).

b. Dry hydrostatic primitive equations prototype

Encouraged by results from the 2-d prototype, CMC and MRB management made a strategic decision in April 1993 to jointly develop over the next several years a new model to efficiently satisfy the requirements of operational weather forecasting at all time and space scales. Contrary to past practices, it was decided that CMC personnel would actively participate in the development of the new-generation model from the very beginning, rather than only becoming involved after its completion, with a view to both accelerating its development and facilitating the transfer of this new technology between MRB research and CMC operations. To this end, one of us from CMC was assigned to work with the four RPN staff members who had already started the formulation of a baroclinic prototype, and coding of this prototype commenced in June 1993. A second person from CMC was subsequently added to this R&D team in March 1994. A first prototype for the dry primitive equations was developed which, together with some preliminary results, was documented in January 1995 and published as Côté et al. (1996).

c. Full-fledged hydrostatic primitive equations model

By January 1996 this dry prototype had been generalized (its formulation is summarized in Section 6) to the moist hydrostatic primitive equations with a comprehensive parameterization of physical processes. After some refinement, testing, and validation, it was decided on 17 May 96 to: (a) complete as soon as possible the development of the model infrastructure (model post processing programs etc.); and (b) deliver the model in Sept 96 for an evaluation by CMC

Operations as to its fitness to replace the Regional Finite Element model for operational forecasting to 48h.

d. Short-range regional configuration

On 27 Sept 96 the joint MRB/CMC committee (CPOP) responsible for authorising changes to both the operational and pre-implementation parallel runs at CMC decided, after reviewing the presented evidence, that the regional configuration of the GEM model should be run twice daily in a CMC pre-implementation run for evaluation of its forecast performance by CMC Operations. A scant two months later, a remarkably short period of time given the complexity of the task, the forecasts became available for evaluation by CMC Operations starting on 1 Dec 96. During this two-month time period further development of the model infrastructure continued. Also a significant code optimisation effort took place, including parallelization of a significant fraction of the model code, which led to the model execution time meeting the real-time operational constraints in a test performed on 23 Dec 96. On 7 Feb 97, CPOP accepted the recommendation of CMC Operations to operationally implement the regional configuration of the GEM model as soon as CMC Implementation was in a position to do so. After introducing the remaining forecast post-processing jobs for CMC clients, the GEM model operationally replaced the Regional Finite Element model on 24 Feb 97.

e. Medium-range configuration

Starting in March 1996, and concurrent with the validation of the short-range configuration of the model, a number of medium-range integrations at uniform resolution were run from time to time and evaluated. Since 1 Oct 96, a medium-range configuration of the model has been systematically run once per day in an "in-house" parallel run with a view to both (a) accelerating the validation and evaluation of the model as a replacement of the operational spectral model for medium-range forecasting; and (b) accumulating model forecast statistics to specify the background error covariance matrices needed in variational data assimilation (e.g. Rabier et al. 1997). Based on evidence accumulated from this "in-house" evaluation run, CPOP decided on 10 Dec 96 that

CMC should introduce this "medium-range" configuration of the model into an official CMC parallel run for evaluation purposes as soon as possible after operational implementation of the regional configuration.

f. Tangent linear model and its adjoint

As noted in Section 4, the more promising four-dimensional data-assimilation techniques require the tangent linear model (TLM), and its adjoint, of the underlying atmospheric forecast model to be available. In anticipation of this need, some preliminary work on the semi-Lagrangian aspects of this, described in Polavarapu et al. (1995) and Tanguay et al. (1997), started in the Fall of 1994. By early 1996, our MRB colleagues Saroja Polavarapu and Monique Tanguay had developed the TLM and its adjoint for the evolved version of the barotropic shallow-water prototype. This TLM was subsequently used in the Polavarapu and Tanguay (1997) study to examine the linearization of iterative processes in the context of four-dimensional data assimilation. In September 1996, work started on developing the TLM and its adjoint for the above-mentioned full-fledged hydrostatic primitive equations model. A first version of this was completed in early January 1997 and further work is underway.

g. Coupled data assimilation system

Work started in the Spring of 1996 on coupling the new model with a 3-dimensional variational data analysis scheme, newly developed (Gauthier et al. 1996) by some of our colleagues in MRB's Satellite Data & Data Assimilation Division and the CMC. Using the incremental approach (Courtier et al. 1994), a first version of the resulting data-assimilation system materialized in December 1996, thanks to the efforts of Stephane Laroche, José Morneau and Pierre Gauthier. Further development, validation, and evaluation of this coupled system is proceeding with a view to an eventual operational implementation.

6. MODEL FORMULATION

a. Governing equations

At the present stage of development, the governing equations are taken to be the forced hydrostatic primitive equations. In the absence of forcing, these equations govern the flow of a frictionless adiabatic shallow hydrostatic fluid on a rotating sphere. A terrain-following hybrid coordinate is defined as

$$\eta \equiv \frac{p - p_T}{p_S - p_T} \equiv \frac{p^* - p_T^*}{p_S^* - p_T^*}, \quad (6.1)$$

where

$$p^* = p_T^* + (p_S^* - p_T^*)\eta, \quad (6.2)$$

p is pressure, p_S and p_T are its respective values at the bottom and top of the atmosphere, and p_S^* and $p_T^* \equiv p_T$ are the respective bottom and top constant pressures of a motionless isothermal ($T^* \equiv \text{constant}$) reference atmosphere. Eq. (6.2) is a direct consequence of the definition (6.1) of the vertical coordinate, and permits the thermodynamic equation to be written in such a way as to ensure the computational stability of the gravitational oscillations. The governing equations in this coordinate system are thus:

$$\frac{d\mathbf{V}^H}{dt} + R_d T_v \nabla \ln p + \nabla \phi + f(\mathbf{k} \times \mathbf{V}^H) = \mathbf{F}^H, \quad (6.3)$$

$$\frac{d}{dt} \ln \left| \frac{\partial p}{\partial \eta} \right| + \nabla \cdot \mathbf{V}^H + \frac{\partial \dot{\eta}}{\partial \eta} = 0, \quad (6.4)$$

$$\frac{d}{dt} \left[\ln \left(\frac{T_v}{T^*} \right) - \kappa \ln \left(\frac{p}{p^*} \right) \right] - \kappa \dot{\eta} \frac{d}{d\eta} (\ln p^*) = F^{T_v}, \quad (6.5)$$

$$\frac{dq_v}{dt} = F^{q_v} \quad (6.6)$$

$$\frac{\partial \phi}{\partial \eta} = -R_d T_v \frac{\partial \ln p}{\partial \eta}, \quad (6.7)$$

where

$$p = \rho R_d T_v, \quad (6.8)$$

and

$$\frac{d}{dt} = \frac{\partial}{\partial t} + \mathbf{V}^H \cdot \nabla + \dot{\eta} \frac{\partial}{\partial \eta}, \quad (6.9)$$

is the substantive derivative following the fluid. Here, \mathbf{V}^H is horizontal velocity, $\phi \equiv gz$ is the geopotential height, ρ is density, T_v is virtual temperature, $\kappa = R_d / c_{pd}$, R_d is the gas constant for dry air, c_{pd} is the specific heat of dry air at constant pressure, q_v is specific humidity of water

vapour, f is the Coriolis parameter, \mathbf{k} is a unit vector in the vertical, g is the vertical acceleration due to gravity, and \mathbf{F}^H , F^{T_v} , and F^{a_v} are parameterized forcings (see below). Eqs. (6.3)-(6.6) are respectively the horizontal momentum, continuity, thermodynamic, and moisture equations, and (6.8) is the equation of state, taken here to be the ideal gas law. The prognostic vertical momentum equation of the fully-compressible Euler equations has been reduced to the diagnostic hydrostatic equation (6.7).

b. Boundary conditions

The boundary conditions are periodicity in the horizontal; and no motion across the top and bottom of the atmosphere, where the top is at constant pressure p_T . Thus

$$\dot{\eta} \equiv \frac{d\eta}{dt} = 0 \text{ at } \eta = 0, 1. \quad (6.10)$$

c. Transport equations

To the above set of governing equations are appended transport equations for various ancillary quantities. These are taken in the form

$$\frac{d\Psi_i}{dt} = F^{\Psi_i}, \quad (6.11)$$

as in Dastoor and Pudykiewicz (1996), where Ψ_i is the i 'th atmospheric tracer and F^{Ψ_i} is its parameterized forcing. Example atmospheric tracers include cloud liquid water and chemical species such as ozone, hydrocarbons and aerosols. The advective form (6.11) of the transport equations are equivalent to the flux form

$$\frac{\partial}{\partial t}(\rho\Psi_i) + \nabla_3 \cdot (\rho\Psi_i\mathbf{V}_3) = \rho F^{\Psi_i}, \quad (6.12)$$

where ∇_3 and \mathbf{V}_3 are respectively the three-dimensional gradient operator and velocity vector.

d. Temporal discretization

Eqs. (6.3)-(6.7) are first integrated in the absence of forcing, and the parameterized forcing terms appearing on the right-hand sides of (6.3)-(6.6) are then computed and added using the usual fractional-step time method (Yanenko 1971).

The time discretization used to integrate the frictionless adiabatic equations of the first step is fully-implicit/ semi-Lagrangian. Consider a prognostic equation of the form

$$\frac{dF}{dt} + G = 0, \quad (6.13)$$

where F represents one of the prognostic quantities $\{\mathbf{V}^H, \ln|\partial p/\partial \eta|, \ln(T/T^*) - \kappa \ln(p/p^*)\}$, and G represents the remaining terms, some of which are nonlinear. Such an equation is approximated by time differences and weighted averages along a trajectory determined by an approximate solution to

$$\frac{d\mathbf{x}_3}{dt} = \mathbf{V}_3(\mathbf{x}_3, t), \quad (6.14)$$

where \mathbf{x}_3 and \mathbf{V}_3 are the three-dimensional position and velocity vectors respectively. Thus

$$\frac{(F^n - F^{n-1})}{\Delta t} + \left[\left(\frac{1}{2} + \varepsilon \right) G^n + \left(\frac{1}{2} - \varepsilon \right) G^{n-1} \right] = 0, \quad (6.15)$$

where $\psi^n = \psi(\mathbf{x}_3, t)$, $\psi^{n-1} = \psi[\mathbf{x}_3(t - \Delta t), t - \Delta t]$, $\psi = \{F, G\}$, $t = n\Delta t$.

Note that this scheme is decentered along the trajectory as in Rivest et al. (1994), to avoid the spurious resonant response arising from a centred approximation in the presence of orography. The off-centering parameter ε is currently set to 0.1 for the operational regional configuration. Cubic interpolation is used everywhere for upstream evaluations (cf. 6.15) except for the trajectory computations (cf. 6.14), where linear interpolation is used with no visible degradation in the results.

Grouping terms at the new time on the left-hand side and known quantities on the right-hand side, (6.15) may be rewritten as

$$\left[F + \left(\frac{1}{2} + \varepsilon \right) \Delta t G \right]^n = \left[F - \left(\frac{1}{2} - \varepsilon \right) \Delta t G \right]^{n-1}. \quad (6.16)$$

This yields a set of coupled nonlinear equations for the unknown quantities at the meshpoints of a regular grid at the new time t , the efficient solution of which is discussed below. A fully-implicit time treatment, such as that adopted here, of the nonlinear terms has the useful property of being inherently computationally more stable than an explicit one (see e.g. the Gravel et al. 1993 analysis).

e. Spatial discretization

A variable-resolution cell-integrated finite-element discretization on an Arakawa C grid is used in the horizontal with a placement of variables as shown schematically in Fig. 6. The vertical discretization is modeled after that of Tanguay et al. (1989).

f. Solving the coupled nonlinear set of discretized equations

After spatial discretization the coupled set of nonlinear equations still has the form of (6.16). Terms on the right-hand side, which involve upstream interpolation, are evaluated once and for all. The coupled set is rewritten as a linear one (where the coefficients depend on the basic state) plus a perturbation which is placed on the right-hand side and which is relatively cheap to evaluate. The linear set can be algebraically reduced to the solution of a three-dimensional elliptic-boundary-value problem. The nonlinear set is then solved iteratively using the linear terms as a kernel, and the nonlinear terms on the right-hand side are re-evaluated at each iteration using the most-recent values.

g. Physical parameterization

To close the problem, the source, sink and redistribution terms of the right-hand sides of (6.3)-(6.6) must be specified or parameterized. These forcings are associated with both unrepresented and sub-grid-scale phenomena. The GEM model has therefore been interfaced with the unified RPN physics package, and a recent description of its contents may be found in Mailhot et al. (1997). Parameterizations are available in this package for the following physical phenomena:

- turbulent fluxes of momentum, heat and moisture over land, water, and ice, based on prognostic turbulent kinetic energy;
- surface-layer effects;
- gravity-wave drag;
- prognostic clouds;
- solar and infrared radiation with or without cloud interaction;

- deep and shallow convection;
- condensation; and
- precipitation including evaporative effects.

h. Digital filter diabatic finalization

Digital filtering is proving to be a good method for the diabatic initialization of weather forecast models (Lynch and Huang 1994). For the model described here, the digital filtering diabatic finalization technique described in Fillion et al. (1995) is used to filter out high-frequency oscillations having periods smaller than 6h. A 6-h forward integration of the complete model, including all the diabatic forcing terms, generates a time series of model states. These are filtered as this 6-h integration progresses in time leading to a noise-free state that is valid 3 h into the integration. The model is then integrated forward in time in the usual way by restarting the integration at 3 h using this time-filtered state.

7. VALIDATING THE STRATEGY FOR CONTINENTAL-SCALE REGIONS (1)

a. Methodology

A preliminary assessment of the global variable-mesh strategy for continental-scale regions was made in Côté et al. (1996) by comparing uniform- and variable-resolution 48-h integrations started from the same initial data, using the methodology introduced in Côté et al. (1993) for the validation of the shallow-water prototype. All of the Côté et al. (1996) integrations were performed using the dry primitive equations in the absence of topography and also in the absence of heat and momentum fluxes. These experiments were then repeated in Staniforth (1997) but at higher (0.8° vs. 1.2°) resolution. In all these studies it was concluded that the 48-h variable-resolution forecast over the uniform-resolution continental window can be well reproduced at a fraction of the cost of using the same uniform resolution everywhere.

The same validation methodology is adopted here. However the GEM model now includes topography and all the physical parameterizations used operationally for regional forecasting, and the experiments are performed at substantially-higher (0.36°) resolution. Ideally they should be run at the 0.33° resolution of the uniform-resolution window of the operational regional mesh displayed in Fig. 2. Unfortunately computer memory limitations do not permit running the uniform-resolution control forecasts at quite such a high resolution at the present time. The experimental methodology is now described in more detail.

Three 48-h integrations are made starting from the same initial data, the Canadian Meteorological Centre analysis valid at 12 UTC 14 Nov 95. This is one of the standard cases used by the CMC to validate regional models before operational implementation, and the strong upstream inflow in the eastern Pacific is of particular interest here. A digital filtering technique based on that described in Fillion et al. (1995) is employed in all experiments to put the fields in dynamic balance, and all integrations were performed with the 28 vertical levels shown schematically in Fig. 7, a timestep of 22.5 mins, and a Laplacian diffusion with a coefficient of $2 \times 10^4 \text{ m}^2 \text{ s}^{-1}$. The three experimental configurations are summarized in Table 1. The purpose of

the two *uniform*-resolution experiments is to validate a uniform-resolution ground truth (Expt. B) against which the *variable*-resolution forecast of Expt. C can be compared and evaluated. Both uniform-resolution experiments were performed at 0.36° resolution (in both longitude and latitude), using either a mesh with the poles of the coordinate system coincident with respect to the geographical ones (Fig. 8a), or rotated (i.e. oriented as in Fig. 8b, but with resolution everywhere uniform).

Expt	Rotated Coordinate System?	Mesh dimensions	Uniform/ Variable	Resolution
A	No	1000 x 500	Uniform	0.36° everywhere
B	Yes, centred on (100°W , 58°N)	1000 x 500	Uniform	0.36° everywhere
C	Yes, centred on (100°W , 58°N)	240 x 268	Variable	0.36° on $59.04^\circ \times 76.68^\circ$ window

Table 1: Experimental configurations.

The variable-resolution Expt. C was performed on the mesh depicted in Fig. 8b, where the poles of the coordinate system are rotated with respect to the geographical ones. Its purpose is to demonstrate the thesis that the forecast over the 0.36° uniform-resolution window can be reasonably-well reproduced at a fraction of the cost of using 0.36° uniform resolution everywhere. The resolution of the variable mesh degrades smoothly away in each direction (each successive meshlength is approximately 10% larger than its predecessor) from a $59.04^\circ \times 76.68^\circ$ uniform-resolution (0.36°) window centered on a point of the equator of a rotated coordinate system, located at (100°W , 58°N) in geographical coordinates. Uniform resolution again refers to uniform spacing in latitude and longitude: however the meshpoints of the window are also almost uniformly spaced over the sphere with a meshlength that varies between approximately 31 and 40 km.

b. Uniform-resolution experiments

The 500-hPa height and mean-sea-level pressure (mslp) fields of the initial analysis used for the experiments are shown in Fig. 9. The resulting 2-day forecasts of these fields for Expts. A and B (i.e. using uniform 0.36° resolution on the unrotated and rotated meshes) are respectively shown in Figs. 10 and 11. The global r.m.s. forecast differences (computed after interpolating the forecast of Expt. A to the rotated mesh of Expt. B) are 4.44 m and 0.58 hPa respectively, showing that the effect of rotating the mesh by 83.37° along a meridian while keeping its resolution uniform is acceptably small.

c. Variable-resolution experiment

The integration of Expt. B (i.e. uniform resolution everywhere in the rotated coordinate system) is considered to be the ground truth for the purposes of validating the 48h forecast of the variable-resolution integration (Expt. C): the meshes of both integrations are identical over the uniform-resolution window of Fig. 8b. The 2-day variable-resolution forecast is shown in Fig. 12 and may be compared to that of the control (Fig. 11). The two forecasts (Expts. B vs. C) are quite close over the uniform-resolution area of interest (defined by the curvilinear rectangle of Fig. 12a). This confirms the thesis that the forecast over the 0.36° uniform-resolution window can be well reproduced at a fraction of the cost of using 0.36° uniform resolution everywhere. However they are significantly different over areas of low resolution, as indeed they should be. The differences (see Fig. 13) between the forecasts of Expts B and C increase as a function of distance from the boundary of the uniform-resolution window, consistent with theory. Quantifying this, the global r.m.s. differences between the forecasts of Expts. B and C are 42.3 m and 3.85 hPa for the 500 hPa height and mslp fields respectively, whereas they are only 5.24 m and 0.48 hPa over the curvilinear rectangle, where the meshpoints of the two grids are coincident. These latter differences are of the same order as those (3.85 m and 0.66 hPa respectively) between Expts A and B computed over the same curvilinear rectangle, which both use the same uniform-resolution meshes but rotated with respect to one another.

d. Comparison of forecasts against analyses

Experiments A to C are designed to test the thesis that a 48-h control forecast obtained using uniform-resolution everywhere can be well reproduced over the uniform-resolution window of a variable-resolution integration, but at a fraction of the cost. This is a numerical sensitivity test. Consequently it does not measure the actual quality of any of the forecasts, only their closeness to one another. To examine the quality of the forecasts displayed in Figs. 10-12, they can be compared with the corresponding verifying analyses shown in Fig. 14. It is seen that forecast quality is generally quite good, albeit with room for improvement, and this is quantified in Table 2 over the $59.07^\circ \times 77.22^\circ$ window of interest. Note that the MSL pressure errors in mountainous regions are spuriously large due to the use of different MSLP-reduction algorithms. All reductions for the models' forecasts were performed using the same newer reduction algorithm, whereas the model reduction used to provide the trial field for the analysis was done with the older much-criticized one. In the future, this inconsistency in the use of MSLP reduction algorithms will be eliminated by also using the newer algorithm in the data assimilation cycle.

Forecast	500 hPa height (m)	MSLP (hPa)
Expt A (Uniform-res unrotated mesh)	22.10	3.11
Expt B (Uniform-res rotated mesh)	22.35	3.20
Expt C (Variable-res rotated mesh)	22.86	3.27
RFE model	23.29	3.44

Table 2: Rms errors, over the $59.07^\circ \times 77.22^\circ$ uniform-resolution window of Fig. 8b, of 48-h forecasts of 500 hPa height and MSL pressure for Expts A, B, C and the RFE model, where the analysis is taken as truth.

e. Comparison of forecasts against those of the RFE model

It is also of interest to compare the quality of the variable-resolution forecasts (Fig. 12) of Expt C with the corresponding ones displayed in Fig. 15 for the RFE (Regional Finite Element) model in its formerly-operational configuration. A priori, the two models are expected to give similar results since: they have approximately the same uniform resolution focused on approximately the same geographical area; they have the same number of vertical levels; and they use the identical set of physical parameterizations.

The forecasts of the GEM and RFE models are indeed quite similar and agree well with the corresponding objective analysis. The main features of the 500 hPa geopotential height on the objective verifying analysis (Fig. 14a) are well simulated by both the GEM (Fig. 12a) and the RFE (Fig. 15a) models. However, a closer examination reveals that both models underestimate the speed and intensity of the short-wave trough that is superimposed on the large-scale ridge over the western part of Canada. Both forecasts also misplace and underestimate the depth of the low in the Gulf of Alaska (cf. Figs. 12a, 15a, and 14a). The associated MSL pressure features predicted by the GEM (Fig. 12b) and the RFE (Fig. 15b) models also exhibit similar errors over the western part of the domain of interest when compared with the verifying MSLP analysis (Fig. 14b), and are probably due to upstream errors in the initial analysis subsequently propagating downstream. Such analysis errors frequently occur due to a paucity of observational data over the Pacific.

The principal differences between the 500 hPa geopotential height forecasts of the GEM (Fig. 12a) and the RFE (Fig. 15a) models over the eastern part of the area of interest are associated with: (a) the low located just east of James Bay, which is 2 dam deeper in the GEM model's forecast; and (b) the 532 dam closed low east of the southern tip of Greenland defined on both the analysis (Fig. 14a) and the GEM model's forecast (Fig. 12a), but which only appears as an open trough in the RFE model's forecast (Fig. 15a). In both cases the GEM model's forecast is closer to the verifying analysis, and this contributes to the lower 500 hPa rms height errors given in Table 2. The associated MSLP features, shown on Fig. 12b for the forecast from the variable-resolution

GEM model and on Fig. 15b for the RFE model's forecast, also manifest a similar behavior. The GEM model gives a depth and position closer to the verifying analysis (Fig. 14b) for both systems, again explaining the lower MSLP rms error (Table 2) of the GEM model (Expt C) when compared with that of the RFE forecast.

Two factors probably explain the better forecast of the GEM model. First, the GEM model is somewhat more active than the RFE model. This is due to both the lower effective horizontal diffusion of the GEM model, and to the absence of the overly-strong sponge layer present near the top of the RFE model. For the latter, the use of a hybrid vertical coordinate in the GEM model rather than the sigma coordinate of the RFE model, has the virtue of providing coordinate surfaces that are less influenced at upper levels by the horizontal detail of the underlying topography. Second, the GEM model is of global extent. It therefore does not suffer from the presence of the artificial wall of the RFE model in the vicinity of the equator, which is probably located a little too close to the southern boundary of the area of interest.

8. VALIDATING THE STRATEGY FOR CONTINENTAL-SCALE REGIONS (2)

From 1 Dec 1996 until its operational implementation on 24 Feb 1997, the new variable-resolution GEM model was integrated twice daily by the CMC in a pre-implementation run. It was configured to be quite close to that of the formerly-operational Regional Finite Element (RFE) model to facilitate its validation for operational forecasting: forecasts from the two models were compared against one another, and also against analyses and observations. The principal attributes of the two model configurations are summarized in Table 3. Both models are configured to have: almost the same resolution over a N. American window of almost the same size; the same number of vertical levels with almost the same placement; and identical physical parameterization packages. Although there are some differences in the numerical techniques, a priori one would theoretically expect these two models, as configured in Table 3, to perform quite similarly.

In the absence of a 12-hour spinup analysis, initial conditions for the GEM model were provided from a horizontal and vertical interpolation of a lower- and uniform- resolution global

analysis performed on the 16 standard isobaric levels. To better simulate operational conditions, identical observational datasets were used to produce both the global analysis used as initial conditions by the GEM model, and the regional analysis used to integrate the RFE model. Consequently the respective cut-off times at the 0000 and 1200 UTC synoptic times for these datasets were 0150 and 1350 UTC.

Quantitative and qualitative evaluations of these comparative forecasting experiments are respectively given in this and the next section.

At the time of writing, verification statistics are available for one hundred and eighteen 48-h forecasts and these are displayed in [Fig. 16](#). The forecasts from the two models are verified against all radiosonde soundings over the uniform-resolution N. American subdomain. This has the virtue of providing a model-independent measure of the truth, at the following standard isobaric levels: 100, 250, 500, 700, 850, 925 and 1000 hPa. There are approximately 120 soundings available per verification time and a typical station distribution is shown in [Fig. 17](#).

The results indicate that the overall performance of the two models is, as argued above, very similar despite two a priori advantages enjoyed in this comparison by the forecast system based on the RFE model. First, the physical parameterization package was developed and tuned for optimum performance for the RFE model and not the GEM model. Second, the RFE model benefits here from its use of a spin-up analysis (Chouinard et al. 1994) made at high-resolution on its own model grid, whereas the initial conditions for the GEM model are presently obtained from a horizontal and vertical interpolation of a lower- and uniform-resolution global analysis. This lack of a spin-up cycle can be expected to result at initial time in both a less-detailed planetary boundary layer and a tropospheric jet of reduced intensity, and also a longer time for the precipitation rate to attain realistic values during the early part of the forecast period. Both of these two disadvantages of the new model will disappear when: (a) the physical parameterization package is further developed and tuned for the new model; and (b) a regional spin-up data-assimilation cycle, driven by the GEM model and performed directly on its grid, is operationally introduced to provide its initial conditions. This augurs well for the future. It also raises the question of why the GEM

model performs so well despite the two above-mentioned handicaps. Contributing factors include: the new model has somewhat improved resolution upstream over the Pacific, a hybrid vertical coordinate, no stratospheric momentum sponge, and less horizontal diffusion; and the RFE model imposes a spurious wall boundary condition in the equatorial region, which in particular is perhaps a little too close to the southern US, an area with many radiosonde stations.

	RFE model	GEM model
Horizontal mesh	305 x 255 hemispheric	289 x 255 global
High-res North American window	245 x 190	235 x 180
Resolution over high-res window	35 km on a polar-stereographic projection (~ 38-25 km on globe)	0.33° on globe (~ 37-29 km on globe)
Levels	28 sigma	28 hybrid
Spatial discretisation	3D finite element	3D finite element
Time discretisation	3-time-level, semi-implicit/ semi-Lagrangian	2-time-level, implicit/ semi-Lagrangian
Timestep	514 s	1350 s
Horizontal diffusion: - coefficient	∇^2 $\nu = 2 \times 10^4 \text{ m}^2 \text{ s}^{-1}$ (applied twice)	∇^2 $\nu = 2 \times 10^4 \text{ m}^2 \text{ s}^{-1}$ (applied once)
Stratospheric momentum sponge	yes	no
Physics	version 3.4 - with quasi-analysis of surface moisture	version 3.4 - with quasi-analysis of surface moisture
Initial conditions	analysed directly on the RFE mesh using a 12-h regional spin-up data assimilation cycle	horizontally and vertically interpolated from the 400 x 200 Gaussian grid of the global data assimilation cycle
Dynamic balancing	adiabatic implicit normal mode	diabatic digital filter

Table 3: Principal attributes of the formerly-operational RFE and currently-operational GEM model configurations.

9. VALIDATING THE STRATEGY FOR CONTINENTAL-SCALE REGIONS (3)

As was the case for the formerly-operational RFE model, the forecast fields from the pre-implementation runs of the GEM model were saved at 3-h intervals during the 48-h forecast period to allow direct comparisons with both the equivalent fields of the RFE model and the verifying analyses and observations. In addition to evaluating a series of objective verification measures to compare GEM and RFE model output forecasts and post-processed products against observed data, a regular assessment of the relative performance of the GEM and RFE models was made by the CMC operational meteorologists. This latter assessment is of course essential to ascertain the day-to-day performance of a new model for the prediction of those features that are significant to real-time daily weather forecasting activities. For this reason, attention was focused mostly on: positions and depths of significant weather systems and associated vertical structures; temperature regimes; upper level jetstreams; boundary layer features; and precipitation forecasts, including both type and amount.

The subjective evaluation of the CMC operational meteorologists is first summarized, followed by more detailed comments on points of particular interest to field forecasters.

a. Summary of the subjective evaluation.

In general, the mass field forecasts of the GEM model do not differ significantly from those of the RFE model, and for the few cases where the differences were significant, neither of the two model forecasts was judged to be superior to the other. This is not overly surprising since the configuration of the GEM model was chosen to be as close as possible to that of the formerly-operational RFE model to facilitate validation of the new model. Although there has only been a few cases where relatively large differences between the model forecasts have been noticed, day-to-day integrations have revealed more subtle differences that are systematic enough to allow characterization of the typical behavior of the GEM model with respect to the operational RFE model. Unless otherwise noted, differences between forecasts increase with the forecast time except quite early in the integration, for reasons explained later in this section.

b. Mean sea-level pressure, geopotential, and weather systems.

The surface lows forecast by the GEM model are often somewhat deeper than those of the RFE model, with differences in central pressure of typical surface lows ranging from 2 hPa to as much as 6 hPa deeper, but it should not be inferred from this that the GEM model systematically develops lows more than the RFE model does. There was a number of cases (including a significant east coast system) where the GEM model developed a low less than the RFE model did and thereby verified better.

For the position and depth of systems, the GEM model's forecasts generally verify a little better than those from the RFE model, albeit by a relatively narrow margin. Deep lows will mostly be better forecast by the GEM model than by the RFE model. It is particularly interesting to note that on several occasions where the GEM model forecast a deeper low, it also correctly moved the low faster than the RFE model. A priori this behavior is perhaps somewhat surprising since strongly-developing systems tend to occlude faster and hence slow down. On those occasions when the GEM model forecast the low to both deepen more and move faster, the occlusion process was correctly forecast to occur earlier by the GEM model than by the RFE model.

It has also been observed that the GEM model often forecasts the upper-air winds to be slightly stronger, and upper-air features to move a little faster, than does the RFE model. In particular, the GEM model forecasts more intense jetstreams. This behavior is systematic enough to be quite noticeable in the vertical profiles of the wind bias of the GEM and RFE forecast verifications displayed in [Fig. 16](#): the winds forecast by the GEM model are on average 1 knot stronger than those forecast by the RFE model. The increased phase speeds of the main tropospheric features and the somewhat stronger winds observed in the GEM model forecasts are probably due to the absence of a strong stratospheric sponge and less horizontal diffusion in the GEM model configuration when compared to that of the RFE model.

During the early part of January, there were periods when significant differences were observed over the western continent in the height and wind fields above 500 hPa, particularly for systems moving in from the edge of or outside the uniform-resolution core of the RFE model grid.

More often than not, these situations were better forecast by the GEM model. A probable contributing factor for this better performance is the somewhat improved resolution in the mid-Pacific of the global analysis feeding the GEM model in these specific situations. During this same early-January period, there has been a number of cases in which the RFE model exhibited a significant negative bias of the geopotential forecasts in the middle and upper troposphere that was not as great in the GEM model's forecasts.

Cold and warm fronts are also sometimes pushed slightly faster by the GEM model than by the RFE model, and the associated troughs are also of course moved slightly faster. This behaviour in these situations is consistent with the GEM model forecasting stronger systems and displacing them faster. This is evident in the low-level thickness patterns forecast by both models, with the GEM model verifying better in many situations.

c. Temperature and humidity.

The temperature field produced by the GEM model is slightly warmer in the middle troposphere when compared to upper air observations than is the RFE model one (Fig. 16), but this signal is far from apparent in the day-to-day comparative evaluation of model forecasts. Of particular interest in Fig. 16 is the significantly-different bias profiles for the dewpoint depression field (particularly at longer time ranges), with the GEM model seeming to give too dry a forecast when compared to both that of the RFE model and the verifying observations. However care must be exercised with dewpoint depression forecasts since a given difference is far more significant when it occurs for low values of dewpoint depression (i.e. for moist areas) than for high ones (i.e. for dry areas). Only minor differences, much smaller than those appearing in Fig. 16, have been observed for humid areas associated with weather systems. In dry areas, the dewpoint depressions forecast by the GEM model are quite often slightly larger than those of the RFE model. For a number of cases where dry slots were forecast to develop in association with significant deepening of a system, the slot was drier in the GEM forecast than in the RFE one. Note that the moisture variable carried by both models is specific humidity. Variables such as

dewpoint depression and relative humidity are obtained by post-processing the variables internally represented in the model, such as specific humidity, using appropriate thermodynamic relations. Because the GEM model atmosphere is slightly warmer in the middle troposphere than its counterpart, this partially explains the differences in the dewpoint depression biases of the two models.

d. Precipitation.

Since precipitation is one of the most important variables forecast by modern numerical-weather-prediction models, special attention was devoted to this field during the evaluation period. A thorough assessment of this highly-discontinuous field requires observational data in both quantity and quality that far surpasses that available to us. Moreover, precipitation at mid-latitudes exhibits a seasonal cycle. In winter it is primarily associated with major synoptic systems, whereas it is predominantly convectively driven in summer. Although intense convective activity does occur in winter at mid-latitudes, it mostly does so over oceanic areas (e.g. over the Gulf Stream) with few verifying observations.

Precipitation forecasts produced by both the GEM and RFE models have been compared between themselves as well as with all the available observations (including radar charts) for various time periods and time ranges. Overall, the GEM model forecasts slightly less precipitation than the RFE model, and this is particularly so for the early (0-6 h) time period.

That the GEM model generally forecasts less precipitation during the early hours of the integration is not surprising. The lack of a spinup data-assimilation cycle can be expected to lead to a longer time for the precipitation rate to attain realistic values than for the RFE model, which has benefited from a 12-h spinup cycle (Chouinard et al. 1994). Depending on the synoptic situation, it takes 6-9 h for the precipitation rates in the GEM model to reach values comparable to those of the RFE model. Thus the 0-12 h accumulated precipitation amounts forecast by the GEM model are generally (but not always) smaller than those forecast by the RFE model, with the differences for the most part being confined to the first 6-h period. The 0-12 h differences can at times reach

15-20% of the maximum value forecast within a precipitation system, and this typically occurs for events where there is significant convective precipitation.

The overall precipitation envelopes (defined here to be the area enclosed by the 1 mm water-equivalent isohyet) forecast by the two models are in general fairly similar. However that of the GEM model tends often (but not always) to be slightly less extensive than that of the RFE model. Although the RFE model tends to overforecast trace precipitation, at Canadian latitudes it does so more during the summer than for a wintertime period such as that of the parallel run evaluated herein. There has been a number of cases where the slightly smaller envelope of the GEM model's forecast better fit the available precipitation observations, but there has also been a number of cases where widespread light precipitation resulting in small snow accumulations (i.e. a trace or so) over large areas was better handled by the RFE model.

The precipitation maxima forecast by the GEM model are often lower than those of the RFE model. This is particularly so for situations where convective precipitation is important with smaller differences occurring if purely stratiform precipitation is forecast by both models. For significant precipitation events associated with synoptic developments (and particularly if convection is present), the precipitation maxima and the envelope of the most significant isohyets are both often forecast by the RFE model to be larger. Often (but not always) the RFE model's forecast has been assessed to be marginally better than that of the GEM model, but the difference is generally small unless deep convection is involved. For the latter case involving deep convection, there is generally no indication that the precipitation forecast of either model is superior to that of the other, only that they are different.

For wintertime synoptic or convective systems that develop over the Gulf Stream or in the northern part of the Gulf of Mexico, the precipitation amounts forecast by the RFE model can be twice as large as those of the GEM model and this difference appears to be greatest for the 36-48 h time period. Although there is very little data to verify these cases, the RFE model's precipitation forecasts look unrealistically high for a quite significant proportion of them, and it is therefore far from clear that this behaviour is desirable. This tendency of the RFE model to forecast more

convective precipitation than the GEM model appears to be correlated with the reduction of the filtering introduced in Oct 1996 in the last version of the formerly-operational RFE model. During the evaluation phase of this last version, it was noted that the precipitation maxima in convective precipitation situations could be up to 30% larger than for the preceding version of the RFE model. Since the GEM model was configured to be as close as possible to that of the preceding version of the RFE model rather than the last one, this probably explains why the last version of the RFE model predicted larger precipitation amounts in convective situations than the GEM model did.

For the few situations that occurred during the evaluation period where several precipitation types were associated with a weather system, the precipitation type diagnosed from the GEM model's vertical temperature structure was evaluated as being slightly better than that of the RFE model. The sample of cases is however very small, and no definite conclusion can be drawn.

e. Statistical and SCRIBE forecasts.

The statistical forecasts (FXCN09) post-processed from the GEM model outputs generally show, for 3-hourly forecast temperatures and also for the probability of precipitation, slightly better skill than the equivalent ones based on the RFE model. About two percentage points more variance is explained by the GEM model, especially at longer time ranges. The statistical forecasts based on the GEM model are also more discriminating inasmuch as they are more likely to predict values at the extremes of the predictand spectrum. These forecasts are derived using a perfect-prog approach, in which most of the predictors used in the regression equation are directly related to the mass fields of the model, which are forecast slightly better by the GEM model. It is therefore to be expected that statistical forecasts based on the GEM model should also verify a little better.

f. The first hours of integration.

The lack of a spinup cycle combined with the low vertical resolution of the global isobaric analysis feeding the GEM model contributes at initial time to both a reduction in intensity of the tropospheric jet, and to a poor definition of the planetary boundary layer. Although these features have not been thoroughly assessed, the early-time evolution of the forecast has been examined

from time to time. The initial-time boundary-layer structure of the GEM model is often significantly different from that of the RFE model. This, not surprisingly, is particularly so for the surface and near-surface fields such as temperature due to: the absence of a spinup model atmosphere at initial time; the low vertical resolution in the analysis provided to the GEM model; and to some small differences in the topographies of the two models. Nevertheless, after only 3 h of integration, the near-surface vertical structure of the GEM model's forecasts have already significantly adjusted towards that of the RFE model which has benefited from a 12-h spinup cycle prior to model integration. This is important to note, since direct comparison of the GEM initial conditions with observational data at initial time can easily lead to erroneous conclusions. This handicap will disappear when a regional data assimilation cycle, driven by the GEM model, is introduced.

10. A MESO-GAMMA-SCALE FEASIBILITY SIMULATION

To demonstrate the proof-of-concept of the variable-resolution strategy for simulating events at the meso- γ scale, the GEM model is integrated to simulate the downslope windstorm (locally termed a "suete") over Cape Breton island described in Benoit et al. (1997), hereinafter referred to as B97. Based on a Froude number analysis and a comparison of hydrostatic and non-hydrostatic integrations at 2-km horizontal resolution, these authors concluded that non-hydrostatic effects for this particular event are relatively unimportant and that a hydrostatic model can be expected to give a realistic simulation. The interest in the present work is *not* to provide a detailed and accurate hindcast of the windstorm (an objective that would in any case be very much limited by the paucity of mesoscale initial and verifying data), but rather to concretely demonstrate the numerical feasibility of using a global variable-resolution model for meso- γ -scale simulation.

a. Synoptic situation

The synoptic situation described in detail in B97 is now briefly summarized. Between 12 UTC Dec 21 1993 and 12 UTC the following day, an initial 992 hPa surface low-pressure system located in the Delaware Bay region moved north-eastward to Quebec and deepened to 973 hPa (see

Fig. 16 of B97). Strong south-easterly winds developed ahead of the warm sector over Nova Scotia leading to the onset of the downslope suete windstorm observed (see the heavy solid curve of Fig. 18 of the present work) from 20 UTC Dec 21 to approximately 09 UTC Dec 22 by the automatic station located at Grand Étang on the western lee side of the Cape Breton Highlands. A frontal trough swept across Nova Scotia around 06 UTC Dec 21, causing the winds to shift from south-easterly to south-westerly and thereby leading to the breakdown of the suete event during the following few hours. At the upstream Sydney (airport) station, the observed wind intensity (see the heavy dashed curve of Fig. 18) is significantly weaker throughout the 24-h period than at the downstream Grand Étang station. Also, the very rapid increase in wind intensity between 20 and 23 UTC Dec 21 observed at Grand Étang is not observed at Sydney.

b. Model configuration

In B97 the MC2 (Mesoscale Compressible Community) model and a nested-grid strategy (with three different resolutions, domains, and integration periods, see their Fig. 17) were used to produce a 7-h simulation (between 21 UTC Dec 21 and 04 UTC Dec 22) of the suete at 2-km horizontal resolution over a domain of size 340 km x 280 km with 25 vertical levels.

A much simpler single-mesh strategy is employed here to simulate the suete at 0.02° (~ 2.2 km) horizontal resolution over a three-times-larger ($6^\circ \times 4^\circ \sim 660$ km x 440 km) domain with 28 vertical levels for almost twice the time period (12 h vs. 7 h) starting from the 18 UTC Dec 21 analysis and terminating at 06 UTC 22 Dec. The 200×300 uniform-resolution (0.02°) window of the 329×418 horizontal mesh is displayed in Fig. 19. The principal motivation for choosing to cover a larger area at such a high resolution and integrating for a longer time period than in the B97 study is to better illustrate the point that the global variable-resolution strategy of the GEM model is indeed feasible for simulating very computationally-challenging meso- γ -scale flows under realistic conditions.

The orientation of the mesh is approximately aligned with the upper-level flow and has sufficient extent to ensure that the embedding synoptic-scale flow is well resolved. This is indeed

found to be so with the simulated central pressure of the surface low exactly matching the analysed values of 976 hPa and 973 hPa respectively at 00 UTC and 06 UTC Dec 22. The timestep (1 min) is taken to be twice as long as that of the MC2 model's simulation since the GEM model has a 2-time-level discretization compared to the 3-time-level one of the MC2 model, and therefore both models take time differences over the same interval of time (1 min) and have similar time-truncation errors. The same twenty-eight levels of the operational regional configuration of the GEM model are used with exactly the same set of physical parameterizations, except that the gravity-wave drag and Kuo convective schemes are turned off, and a simple super-saturation removal scheme is used instead of the Sundqvist parameterization. The orography and land-sea mask are obtained from an available high-resolution database, but the surface roughness length had to be interpolated from the 0.33°-resolution operational field. The diffusion coefficient for the present simulation is taken to be $2500 \text{ m}^2\text{s}^{-1}$ for all prognostic variables, comparable to the value of $1920 \text{ m}^2\text{s}^{-1}$ used at 10%-higher horizontal resolution in B97 for all prognostic variables except vertical momentum, for which a five-times-larger value was employed.

c. The simulation

The 10m windspeed and MSL pressure fields, simulated by the GEM model and valid at 03 UTC 22 Dec, are respectively displayed over the Cape Breton Highlands in [Figs. 20-21](#). They are quite similar to the corresponding fields of the B97 integrations (their [Figs. 24 and 20](#)). The incident south-easterly flow coming in from the ocean is altered by the mesoscale reorganization of the circulation over and around Cape Breton, and slowed down by both the enhanced surface drag over the Highlands and the upward slope of the orography to its crest. The flow then sharply accelerates over the very-steep downward slope on the lee side of this crest to produce two strong and narrow near-surface jets ([Fig. 20](#) of the present work), with wind intensities greater than 35 knots and a maximum intensity of 41 knots. These areas of high windspeed are located just offshore and in the north-western lee of the Highlands, and are aligned parallel to the coast.

A mesoscale pressure trough (Fig. 21) has developed along the coast on the northwestern lee side of the mountain crest with an associated mesoscale ridge on the windward side. The simulation also gives a strong mesoscale sea-level drop in pressure across the Highlands of approximately 7 hPa over a horizontal distance of approximately 75 km. Fortuitously, the maximum and minimum simulated pressures respectively occur close to the upstream Sydney and downstream Grand Étang observing stations. The simulated and observed pressure differences between these two stations at 03 UTC Dec 22 are respectively 6.3 hPa and 8.3 hPa, giving credence to the simulation.

The latitude and longitude of the locations of these two observing stations as defined in the World Meteorological Organization Station Dictionary is only given to the nearest minute of arc (~ 2 km). This means that the station locations could in reality be anywhere within a radius of approximately 1 km (~ half the meshlength) or so of that defined by the Station Dictionary, causing a sampling problem. For the MSL pressure field this is not at all serious since sampling the field a half meshlength away from that defined by the dictionary negligibly perturbs the results due to the relative smoothness of this field in the vicinity of the stations. For the windspeed field the problem is more serious. Shifting the station location by a half meshlength at the Grand Étang station can for example change the sampled simulated result at 03 UTC 22 Dec by plus or minus 4 knots, due to the very large gradient of this field at this station in the direction normal to the coast.

Nevertheless, it is still useful to qualitatively compare the simulated 10m windspeed at the stations with that observed. It can be seen from Fig. 18 that the rapid onset of the downslope windstorm at Grand Étang between 20 and 23 UTC Dec 21 is qualitatively well simulated, while no abrupt increase in windspeed occurs at the upstream Sydney station. Quantitatively, the agreement is excellent at the upstream station, for which the sampling of the windspeed is insensitive to a displacement of a half meshlength. For the downstream Grand Étang station, the windspeed is generally somewhat under-estimated. This is not surprising given the above-described sampling error and the limitations of the experiment; e.g. the absence of a mesoscale analysis, the use of a too-smooth definition of roughness length, and the limited resolution.

The results displayed in Fig. 21 of B97 for the MC2 model with 2-km resolution can be compared to those shown in Fig. 18 of the present work for the GEM model at similar resolution. At the upstream Sydney station, the MC2 model's 2-km-resolution integration gives 10m windspeeds (their Fig. 21b) that are significantly in error. The simulated values of the MC2 model are about twice as large as the observed sustained windspeed (i.e. the average value within a gridbox that a model represents), and significantly larger even than the observed gusts. For the downstream Grand Étang station, the MC2 model's simulation again overestimates the sustained windspeed (their Fig. 21a). This overestimation increases throughout the 7-h simulation period such that by the end of the period, the simulated windspeed is 30% larger than that observed.

From the above, it is concluded that it is numerically feasible to use a global variable-resolution model, such as the GEM model, for meso- γ -scale simulations. For physical validity, the model should however employ the non-hydrostatic Euler equations as governing equations, together with appropriate parameterizations of any unrepresented physical processes.

11. VALIDATING THE STRATEGY FOR MEDIUM-RANGE FORECASTING

From 1 Oct 1996 and with only minor changes, the GEM model has been experimentally run once per day with a uniform-resolution configuration suitable for medium-range forecasting. The chosen configuration (see Table 4) is quite similar to that of the currently-operational spectral (SEF) model to facilitate forecast comparisons, but with two significant exceptions. These are: the number of levels (28 for the new model vs. 21 for the spectral model) and their placement; and the set of physical parameterizations (version 3.4 for the new model vs version 3.1 for the spectral model). The justification for these two exceptions is that it is considered desirable, to the extent reasonably possible, to configure the operational medium-range forecast model to have: (a) the same number and placement of vertical levels as the operational short-range regional model; and (b) the same set of parameterizations. This configuration can be expected to confer an advantage to the GEM model in any comparison against the currently-operational SEF model, since it thereby has higher vertical resolution and a more evolved set of physical parameterizations. However for the

comparisons presented here, against this advantage must be weighed the disadvantage that the GEM model uses degraded initial conditions due to the horizontal and vertical interpolation of the analysis. The effect of the horizontal interpolation is relatively unimportant because the two meshes (Gaussian vs uniform lat-lon) are almost identical since a Gaussian grid at high resolution asymptotes towards uniform resolution. The effect of vertical interpolation of the analysis, as discussed in Section 8, is far more serious and leads at initial time to a degraded definition of the planetary boundary layer, a reduction in jet intensity, and a longer precipitation spin-up time. These weaknesses should be addressed when the global data-assimilation system is modified to be driven by the GEM model and to produce analyses directly on the GEM model's 3-d grid.

At the time of writing, verification statistics are available for all 92 cases of the three-month period Oct-Dec 1996. The forecasts from the two models have been verified, at the same set of seven standard levels (100, 250, 500, 700, 850, 925 and 1000 hPa) as in Section 8, against all available radiosonde soundings (approximately 350 per verification time) over the globe (see [Fig. 23](#) for a typical station distribution). The resulting scores, averaged over all cases, are displayed in [Fig. 22](#) for the forecasts to 6 days.

The results indicate that, despite its handicap of using degraded initial conditions, the GEM model performs on average quite similarly to the operational SEF model. The GEM model has: a significantly smaller wind bias and a smaller rms temperature error above 500 hPa (both probably due to better vertical resolution, the use of a hybrid coordinate, and the absence of an overly-strong stratospheric sponge); and a smaller tropospheric moisture bias (probably attributable to the more recent physical parameterization package). On the other side of the ledger however, it has: a larger mid-tropospheric rms moisture error, possibly attributable to differences in the physical parameterization packages; and a larger height bias.

	SEF model	GEM model
Horizontal mesh (resolution)	400 x 200 Gaussian grid (T199 ~ 0.9°)	400 x 200 uniform grid (0.9°)
Levels	21 sigma	28 hybrid
Spatial discretisation	2D spectral + 1D finite element	3D finite element
Time discretisation	3-time-level, semi-implicit/ semi-Lagrangian	2-time-level, implicit/ semi-Lagrangian
Timestep	30 mins	40 mins
Horizontal diffusion - coefficient	∇^2 $v_{\text{average-of-1st-3-days}} = 5 \times 10^4 \text{ m}^2 \text{ s}^{-1}$ <hr/> $v = 2 \times 10^4 \text{ m}^2 \text{ s}^{-1}$ at $t = 0$, linearly increasing to $v = 10^5 \text{ m}^2 \text{ s}^{-1}$ at $t = 4$ days	∇^2 $v = 4.8 \times 10^4 \text{ m}^2 \text{ s}^{-1}$
Stratospheric sponge	yes	no
Physics	version 3.1 - with climatological surface moisture	version 3.4 - with climatological surface moisture
Initial conditions	analysed directly on the 400 x 200 Gaussian grid of the global data assimilation cycle	horizontally and vertically interpolated from the 400 x 200 Gaussian grid of the global data assimilation cycle
Dynamic balancing	adiabatic normal-mode	diabatic digital filter

Table 4: Principal attributes of the spectral (SEF) and global uniform-resolution GEM model configurations for the comparisons.

12. CONCLUSION

To meet the needs of operational weather forecasting and research, as well as those of air-quality and climate modeling, a unified strategy is proposed that is based on the use of a global variable-resolution model, run with different configurations. Broadly speaking, these are:

- (i) a *uniform-resolution 'global-scale'* configuration, for large-scale problems such as medium- and long-range weather forecasting, climate change modeling, and the long-range transport of pollutants;
- (ii) a *variable-resolution 'continental-scale'* configuration for regional-scale problems such as more detailed forecasts to 2 days, and regional air-quality and climate modeling; and
- (iii) *variable-resolution 'provincial-scale'* and *'urban-scale'* configurations for yet-more-detailed forecasts and simulations at correspondingly-shorter time periods.

This approach offers significant economies in both operational and research environments, since there is only one model to maintain, develop and optimize, instead of the usual two or more. It also provides an efficient and conceptually-simple solution to the nesting problem for regional forecasting: the planetary-scale waves are adequately resolved around a high-resolution subdomain (which resolves the smaller-scale disturbances); there are no artificial lateral boundaries with their attendant problems; and there is no abrupt change of resolution across an internal boundary since the resolution varies smoothly away from the area of interest.

Key ingredients of this strategy include:

- (i) a *fully-implicit time treatment of the terms responsible for the fastest-moving acoustic and gravitational oscillations* that carry negligibly-small energy yet unduly restrict the timestep if treated explicitly;
- (ii) a *semi-Lagrangian treatment of advection* to overcome the stability limitations encountered in Eulerian schemes due to the convergence of the meridians and to strong jet streams;
- (iii) a *cell-integrated finite-element spatial discretization* to provide a robust way of achieving variable resolution;

- (iv) an *arbitrarily-rotated latitude-longitude mesh* to focus resolution on any part of the globe, be it mid-litudinal or tropical;
- (v) an *embedded advection-diffusion module* to transport a family of chemical species for air-quality and environmental-emergency-response applications;
- (vi) a *tangent linear model and its adjoint* to facilitate the development of future 4-d data assimilation systems; and
- (vii) the eventual use of the *non-hydrostatic Euler equations* (with a switch to revert to the hydrostatic primitive equations) to maintain the model's validity at scales where the hydrostatic assumption breaks down.

A Global Environmental Multiscale (GEM) model has been constructed based on the described strategy. Experiments confirm the potential of the proposed strategy for a broad range of scales. Medium-range integrations of the GEM model have been run daily over a 3-month period with uniform resolution almost identical with that of CMC's operational spectral model, and it is found that the two sets of forecasts are of comparable quality. For regional forecasting at the continental scale, a controlled set of experiments show that differences between the 48-h forecasts for the 500 hPa geopotential height and mean-sea-level pressure fields obtained from a uniform horizontal resolution integration, and those obtained from a variable-mesh one with equivalent resolution over a N. American window, are acceptably small. Further variable-resolution experiments, including a meso- γ -scale simulation, show that the overhead associated with using a model of global extent for short- and very-short-range forecasting is relatively small, and that the overhead of using variable resolution outside the area of interest is consequently comparable to that of the sponge regions of driven limited-area models. After two-and-a-half months of comparative tests performed under operational conditions, the GEM model replaced CMC's formerly-operational Regional Finite Element model, and it is now run twice daily to provide 48-h forecasts over N. America.

Work is continuing on other aspects of the development, validation, and operational implementation of the GEM forecast and simulation system. These include: generalizing the GEM

model to include non-hydrostatic terms; further developing and validating an associated data-assimilation system driven by the GEM model; preparing to replace the operational spectral model by a uniform-resolution configuration of the GEM model for medium-range forecasting; and working towards ultimately making the GEM model available to the R&D community as a user-friendly tool.

APPENDIX A

Asymptotic properties of a family of variable-resolution meshes

Consider the one-dimensional variable-resolution distribution of $(N^{un} + N^{var} + 1)$ points shown in Fig. 24 for a domain of length $(L^{un} + L^{var})$ having a uniform-resolution sub-domain of length L^{un} , where N^{var} is restricted to be even. There are thus N^{un} intervals in the uniform-resolution sub-domain, and $N^{var}/2$ intervals in each of the two variable-resolution sub-domains. Also, let the resolution in the variable-resolution sub-domains vary such that, moving from the uniform-resolution sub-domain, each successive mesh-length is a fixed-ratio r larger than that of its preceding neighbour, with the first such mesh-length being set to rh , where h is the constant mesh-length of the uniform-resolution sub-domain. Thus, considering the right-most variable-resolution part of the mesh in Fig. 24, the mesh-length to the right of the point with index n is

$$h_n = r^{n+1}h \quad \text{for } n = 0, 1, 2, \dots, (N^{var}/2 - 1). \quad (\text{A1})$$

where

$$h = \frac{L^{un}}{N^{un}}. \quad (\text{A2})$$

With the above definitions, the following constraint must hold:

$$\frac{L^{var}}{2} = rh + r^2h + r^3h + \dots + r^{N^{var}/2}h = \left(\frac{r^{N^{var}/2} - 1}{r - 1} \right) rh. \quad (\text{A3})$$

This may be rewritten as

$$r^{N^{var}/2} - 1 = \frac{C}{h}, \quad (\text{A4})$$

where

$$C = \frac{(r-1)}{2r} L^{var}, \quad (\text{A5})$$

is a constant for a fixed ratio r . Solving (A4) then yields

$$N^{var} = 2 \frac{\ln(1 + C/h)}{\ln r}. \quad (\text{A6})$$

For $r > 1$ and N^{var} large, (A4) asymptotically reduces to

$$r^{N^{var}/2} \approx \frac{C}{h}, \quad (\text{A7})$$

and so asymptotically

$$N^{var} \approx 2 \left(\frac{\ln C - \ln h}{\ln r} \right). \quad (\text{A8})$$

Consider now the question: how many additional points are asymptotically required in the variable-resolution parts of the mesh if the resolution is doubled in the fixed-size uniform-resolution sub-domain, while still maintaining a fixed-ratio r between successive mesh-lengths in the two variable-resolution sub-domains? Now the number of meshpoints $N^{var}(h/2)$ in the variable-resolution parts of the mesh after such a doubling of resolution in the uniform-resolution sub-domain asymptotically goes from the number $N^{var}(h)$ given in (A8) to

$$\begin{aligned} N^{var}\left(\frac{h}{2}\right) &= 2 \left[\frac{\ln C - \ln(h/2)}{\ln r} \right] = 2 \left(\frac{\ln C - \ln h}{\ln r} \right) + 2 \left(\frac{\ln 2}{\ln r} \right) \\ &= N^{var}(h) + 2 \left(\frac{\ln 2}{\ln r} \right). \end{aligned} \quad (\text{A9})$$

Thus, asymptotically, for each successive doubling of resolution in the uniform-resolution sub-domain only an additional $(\ln 2 / \ln r)$ points need to be added in each of the two variable-resolution sub-domains. For $r \approx 1.1$, this means that only an extra 7 points are asymptotically required in each variable-resolution subdomain when doubling the number in the uniform-resolution sub-domain.

From (A6), (A5) and (A2), the ratio of the number of mesh-points in the uniform-resolution sub-domain (including both its endpoints) to the total number may be determined. This ratio will depend upon whether the domain is periodic or not. For a periodic domain, there will be one less total number of points since the left-most and right-most points coalesce into a single point. Thus for a periodic domain the ratio of the number of mesh-points in the uniform-resolution sub-domain (including both its endpoints) to the total number is

$$\frac{N^{un} + 1}{N^{un} + N^{var}} = \frac{(L^{un} + h) \ln r}{L^{un} \ln r + 2h \ln \left[1 + \frac{(r-1) L^{var}}{2r h} \right]}, \quad (\text{A10})$$

whereas for an aperiodic domain it becomes

$$\frac{N^{un} + 1}{N^{un} + N^{var} + 1} = \frac{(L^{un} + h) \ln r}{(L^{un} + h) \ln r + 2h \ln \left[1 + \frac{(r-1) L^{var}}{2r h} \right]}. \quad (\text{A11})$$

Expressions (A10)-(A11) can be used to determine the ratio of the number of mesh-points in the uniform-resolution sub-domain to the total number for the two-dimensional variable-resolution meshes discussed in the body of this paper. Using these and letting subscripts λ and θ respectively denote quantities in the λ and θ directions, then leads to the following expression for this ratio:

$$\left(\frac{N_{\lambda}^{un} + 1}{N_{\lambda}^{un} + N_{\lambda}^{var}} \right) \left(\frac{N_{\theta}^{un} + 1}{N_{\theta}^{un} + N_{\theta}^{var} + 1} \right) = \frac{(L_{\lambda}^{un} + h_{\lambda}) \ln(r_{\lambda}) (L_{\theta}^{un} + h_{\theta}) \ln(r_{\theta})}{\left\{ L_{\lambda}^{un} \ln r_{\lambda} + 2h_{\lambda} \ln \left[1 + \frac{(r_{\lambda} - 1) L_{\lambda}^{var}}{2r_{\lambda} h_{\lambda}} \right] \right\} \left\{ (L_{\theta}^{un} + h_{\theta}) \ln r_{\theta} + 2h_{\theta} \ln \left[1 + \frac{(r_{\theta} - 1) L_{\theta}^{var}}{2r_{\theta} h_{\theta}} \right] \right\}}, \quad (\text{A12})$$

where $L_{\lambda}^{var} = 2\pi - L_{\lambda}^{un}$ and $L_{\theta}^{var} = \pi - L_{\theta}^{un}$.

REFERENCES

- Benoit, R., M. Desgagné, P. Pellerin, S. Pellerin, Y. Chartier, and S. Desjardins, 1997: The Canadian MC2: a semi-Lagrangian, semi-implicit wide-band atmospheric model suited for fine-scale process studies and simulation. *Mon. Wea. Rev.*, accepted.
- Bermejo, R., and A. Staniforth, 1992: The conversion of semi-Lagrangian advection schemes to quasi-monotone schemes. *Mon. Wea. Rev.*, **120**, 2622-2632.
- Caian, M., and J.-F. Geleyn, 1997: Some limits to the variable mesh solution and comparison with the nested LAM one. *Q. J. Roy. Met. Soc.*, accepted.
- Chouinard, C., J. Mailhot, H.L. Mitchell, A. Staniforth, and R. Hogue, 1994: The Canadian regional data assimilation system: operational and research applications. *Mon. Wea. Rev.*, **122**, 1306-1325.
- Côté, J., M. Roch, A. Staniforth, and L. Fillion, 1993: A variable-resolution semi-Lagrangian finite-element global model of the shallow-water equations. *Mon. Wea. Rev.*, **121**, 231-243.
- Côté, J., S. Gravel, A. Méthot, A. Patoine, M. Roch, and A. Staniforth, 1996: Preliminary results from a dry global variable-resolution primitive equations model. *Atmos.-Ocean*, André J. Robert Memorial Symposium issue, to appear.
- Courtier, P., and J.-F. Geleyn, 1988: A global numerical weather prediction model with variable resolution: application to the shallow-water equations. *Q. J. Roy. Met. Soc.*, **114**, 1321-1346.
- Courtier, P., C. Freydiet, J.-F. Geleyn, F. Rabier, and M. Rochas, 1991: The Arpege project at Météo France. *Proc. Numerical Methods in Atmospheric Models*, European Centre for Medium-range Weather Forecasts, Shinfield Park, Reading, UK, 193-231.
- Courtier, P., J.-N. Thépaut, and A. Hollingsworth, 1994: A strategy for operational implementation of 4D-Var, using an incremental approach. *Q. J. Roy. Meteor. Soc.*, **120**, 1367-1388.

- Daley, R., 1991: *Atmospheric Data Analysis*. Cambridge Atmospheric and Space Science Series, vol. 2, Cambridge University Press, 457 pp.
- D'Amours, R., M. Jean, R. Servranckx, J.-P. Toviessi, and S. Trudel, 1995: The operational use of the Canadian emergency response model to solve multi-disciplinary problems. Proc. 5th AES/CMOS Workshop on Operational Meteorology, held Feb 27 - March 3 1995 in Edmonton. G. Vickers and C. McLeod (eds.), Atmospheric Environment Service, 4905 Dufferin St., Downsview, Ontario, Canada M3H 5T4, 207-216.
- Dastoor, A.P., and J. Pudykiewicz, 1996: A numerical global meteorological sulfur transport model and its application to arctic air pollution. *Atmospheric Environment*, **30**, 1501-1522.
- Déqué, M., and J.P. Pielieuvre, 1995: High resolution climate simulation over Europe. *Climate Dynamics*, **11**, 321-339.
- DiMego, G.J., K.E. Mitchell, R.A. Petersen, J.E. Hoke, J.P. Gerrity, J.C. Tuccillo, R.L. Wobus, and H.H. Juang, 1992: Changes to NMC's regional analysis and forecast system. *Wea. Forecasting*, **7**, 185-198.
- Fillion, L., H.L. Mitchell, H. Ritchie, and A. Staniforth, 1995: The impact of a digital filter finalization technique in a global data assimilation system. *Tellus*, **47A**, 304-323.
- Fox-Rabinowitz, M., G. Stenchikov, M. Suarez, and L. Takacs, 1997: A finite-difference GCM dynamical core with a variable resolution stretched grid. *Mon. Wea. Rev.*, submitted, manuscript available from authors.
- Gates, W.L., 1992: AMIP: The Atmospheric Model Intercomparison Project. *Bull. Amer. Meteor. Soc.*, **73**, 1962-1970.
- Gates, W.L. (ed), 1995: The Proceedings of the First International AMIP Scientific Conference, WCRP-92, WMO/TD-No. 732, World Climate Research Programme, World Meteorological Organisation, Geneva, 532 pp.

- Gauthier, P., L. Fillion, P. Koclas, and C. Charette, 1996: Implementation of a 3D variational analysis at the Canadian Meteorological Centre. 11th AMS Conference on NWP, Norfolk, Virginia, 19-23 August 1996, 232-234. American Meteor. Soc., Boston, Mass.
- Gravel, S., and A. Staniforth, 1992: Variable resolution and robustness. *Mon. Wea. Rev.*, **120**, 2633-2640.
- Gravel, S., A. Staniforth, and J. Côté, 1993: A stability analysis of a family of baroclinic semi-Lagrangian forecast models. *Mon. Wea. Rev.*, **121**, 815-826.
- Hardiker, V., 1997: A global numerical weather prediction model with variable resolution. *Mon. Wea. Rev.*, **125**, 59-73.
- Heffter, J.L., and B.J.B. Stunder, 1993: Volcanic ash forecast and dispersion (VAFTAD) model. *Wea. Forecasting*, **8**, 533-541.
- Kasahara, A., 1974: Various vertical coordinate systems used for numerical weather prediction. *Mon. Wea. Rev.*, **102**, 509-522.
- Laprise, R., 1992: The Euler equations of motion with hydrostatic pressure as independent variable. *Mon. Wea. Rev.*, **120**, 197-207.
- Lynch, P., and X.-Y. Huang, 1994. Diabatic initialization using recursive filters. *Tellus*, **46A**, 583-597.
- Mailhot, J., R. Sarrazin, B. Bilodeau, N. Brunet, and G. Pellerin, 1997: Development of the 35-km version of the operational regional forecast system. *Atmos.-Ocean*, **35**, to appear.
- Mitchell, H.L., C. Chouinard, C. Charette, R. Hogue, and S.J. Lambert, 1996: Impact of a revised analysis algorithm on an operational data assimilation system. *Mon. Wea. Rev.*, **124**, 1243-1255.
- Oliger, J., and A. Sundström, 1978: Theoretical and practical aspects of some initial boundary value problems in fluid dynamics. *S.I.A.M. J. Appl.Math.*, **35**, 419-446.
- Paegle, J., 1989: A variable resolution global model based upon Fourier and finite element representation. *Mon. Wea. Rev.*, **117**, 583-606.

- Paegle, J., Q. Yang, and M. Wang, 1997: Predictability in limited area and global models. *Meteor. Atm. Phys.*, accepted.
- Phillips, N.A., 1957: A coordinate system having some special advantages for numerical forecasting. *J. Meteor.*, **14**, 184-185.
- Polavarapu, S., M. Tanguay, R. Ménard, and A. Staniforth, 1995: The tangent linear model for semi-Lagrangian schemes - linearizing the process of interpolation. *Tellus*, **47A**, 74-95.
- Polavarapu, S., and M. Tanguay, 1997: Linearising iterative processes for four-dimensional data assimilation. *Q. J. Roy. Meteor. Soc.*, submitted.
- Priestley, A., 1993: A quasi-conservative version of the semi-Lagrangian advection scheme. *Mon. Wea. Rev.*, **121**, 621-629.
- Pudykiewicz, J., 1989: Simulation of the Chernobyl dispersion with a 3-D hemispheric tracer model. *Tellus*, **41B**, 391-412.
- Rabier, F., A. McNally, E. Andersson, P. Courtier, P. Uden, J. Eyre, A. Hollingsworth, and F. Bouttier, 1997: The ECMWF implementation of three dimensional variational (3D-Var). Part II: Structure functions. *Q. J. Roy. Meteor. Soc.*, submitted.
- Ritchie, H., and C. Beaudoin, 1994: Approximations and sensitivity experiments with a baroclinic semi-Lagrangian spectral model. *Mon. Wea. Rev.*, **122**, 2391-2399.
- Rivest, C., A. Staniforth and A. Robert, 1994: Spurious resonant response of semi-Lagrangian discretizations to orographic forcing: Diagnosis and solution. *Mon. Wea. Rev.*, **122**, 366-376.
- Robert, A., 1981: A stable numerical integration scheme for the primitive meteorological equations. *Atmos.-Ocean*, **19**, 35-46.
- Robert, A., 1982: A semi-Lagrangian and semi-implicit numerical integration scheme for the primitive meteorological equations. *J. Meteor. Soc. Japan*, **60**, 319-325.
- Schmidt, F., 1977: Variable fine mesh in the spectral global models. *Beitr. Phys. Atmos.*, **50**, 211-217.

- Semazzi, F.H.M., J.-H. Qian, and J.S. Scroggs, 1995: A global nonhydrostatic semi-Lagrangian atmospheric model. *Mon. Wea. Rev.*, **123**, 2534-2550.
- Sharma, O.P., H. Upadhyaya, Th. Braine-Bonnaire, and R. Sadourny, 1987: Experiments on regional forecasting using a stretched coordinate general circulation model. *Short- and Medium- Range Numerical Weather Prediction*, Proceedings of WMO/ IUGG NWP Symposium, 263-271, Met. Soc. Japan, Tokyo, T. Matsuno (ed), 831 pp.
- Staniforth, A., 1987: Review - formulating efficient finite-element codes for flows in regular domains. *Int. J. Numer. Meth. Fluids*, **7**, 1-16.
- Staniforth, A., and J. Côté, 1991: Semi-Lagrangian integration schemes for atmospheric models - a review. *Mon. Wea. Rev.*, **119**, 2206-2223.
- Staniforth, A., 1997: Regional modeling: a theoretical discussion. *Meteor. Atmos. Phys.*, accepted.
- Tanguay, M., A. Simard, and A. Staniforth, 1989: A three-dimensional semi-Lagrangian scheme for the Canadian regional finite-element forecast model. *Mon. Wea. Rev.*, **117**, 1861-1871.
- Tanguay, M., A. Robert, and R. Laprise, 1990: A semi-implicit semi-Lagrangian fully compressible regional forecast model. *Mon. Wea. Rev.*, **118**, 1970-1980.
- Tanguay, M., S. Polavarapu, and P. Gauthier, 1997: Temporal accumulation of first-order linearization error for semi-Lagrangian passive advection. *Mon. Wea. Rev.*, **125**, accepted.
- Yanenko, N.N., 1971. *The Method of Fractional Steps*. Springer, New York.

FIGURE LEGENDS

- Fig. 1** The 305 x 255 variable-resolution horizontal grid of the formerly-operational RFE model. It has uniform 35 km resolution over the 245 x 190 central window and, for clarity, only every 5th line of this polar-stereographic mesh is shown.
- Fig. 2 (a)** The 255 x 289 variable-resolution horizontal grid of the currently-operational regional configuration of the GEM model: it has uniform 0.33° resolution over the $59.07^\circ \times 77.22^\circ$ (180×235) central window.
- (b)** As in (a) but viewed from a different perspective.
- Fig. 3** A variable-resolution 427 x 414 *provincial* mesh having a $10^\circ \times 10^\circ$ (304×304) window of uniform 0.033° resolution, centred on (122°W , 53.5°N).
- Fig. 4** A variable-resolution 584 x 569 *urban* mesh having a 150 km x 150 km (413×413) window of uniform 0.0033° resolution, centred on (73.5°W , 45.5°N).
- Fig. 5** The percentage of points located over the uniform-res $59.07^\circ \times 77.22^\circ$ subdomain of the operational regional configuration of the GEM model w.r.t. the total no. of points, as a function of increasing resolution. Dashed line denotes the current operational resolution.
- Fig. 6** Schematic for horizontal placement of variables, displayed around a pole. Squares: scalar fields. Circles: $U = \lambda$ – component of wind images. Diamonds: $V = \theta$ – component of wind images.
- Fig. 7** Vertical mesh over an idealized mountain for the currently-operational regional configuration of the GEM model with 28 levels.
- Fig. 8 (a)** The uniform 0.36° resolution 1000 x 500 mesh used for Expt A.
- (b)** A variable-resolution 240 x 268 mesh having an $59.04^\circ \times 76.68^\circ$ window of uniform 0.36° resolution, centred on (100°W , 58°N), and used for Expt C.

Fig. 9 (a) Initial geopotential height at 500 hPa in dam on an orthographic projection; contour interval = 6 dam.

(b) Initial msl pressure in hPa on an orthographic projection; contour interval = 4 hPa.

Fig. 10 (a) Same as in Fig. 9a, but at 48-h for Expt. A.

(b) Same as in Fig. 9b, but at 48-h for Expt. A.

Fig. 11 (a) Same as in Fig. 9a, but at 48-h for Expt. B.

(b) Same as in Fig. 9b, but at 48-h for Expt. B.

Fig. 12 (a) Same as in Fig. 9a, but at 48-h for Expt. C.

(b) Same as in Fig. 9b, but at 48-h for Expt. C.

Fig. 13 Difference between 48-h forecast of Expt. B and Expt. C on an orthographic projection for:

(a) 500 hPa geopotential height; contour interval = $\pm 1, \pm 3, \pm 5, \dots$ dam.

(b) mslp ; contour interval = $\pm 1, \pm 3, \pm 5, \dots$ hPa.

Fig. 14 (a) Same as in Fig. 9a, but for 48-h verifying analysis.

(b) Same as in Fig. 9b, but for 48-h verifying analysis.

Fig. 15 (a) Same as in Fig. 9a, but for 48-h RFE forecast.

(b) Same as in Fig. 9b, but for 48-h RFE forecast.

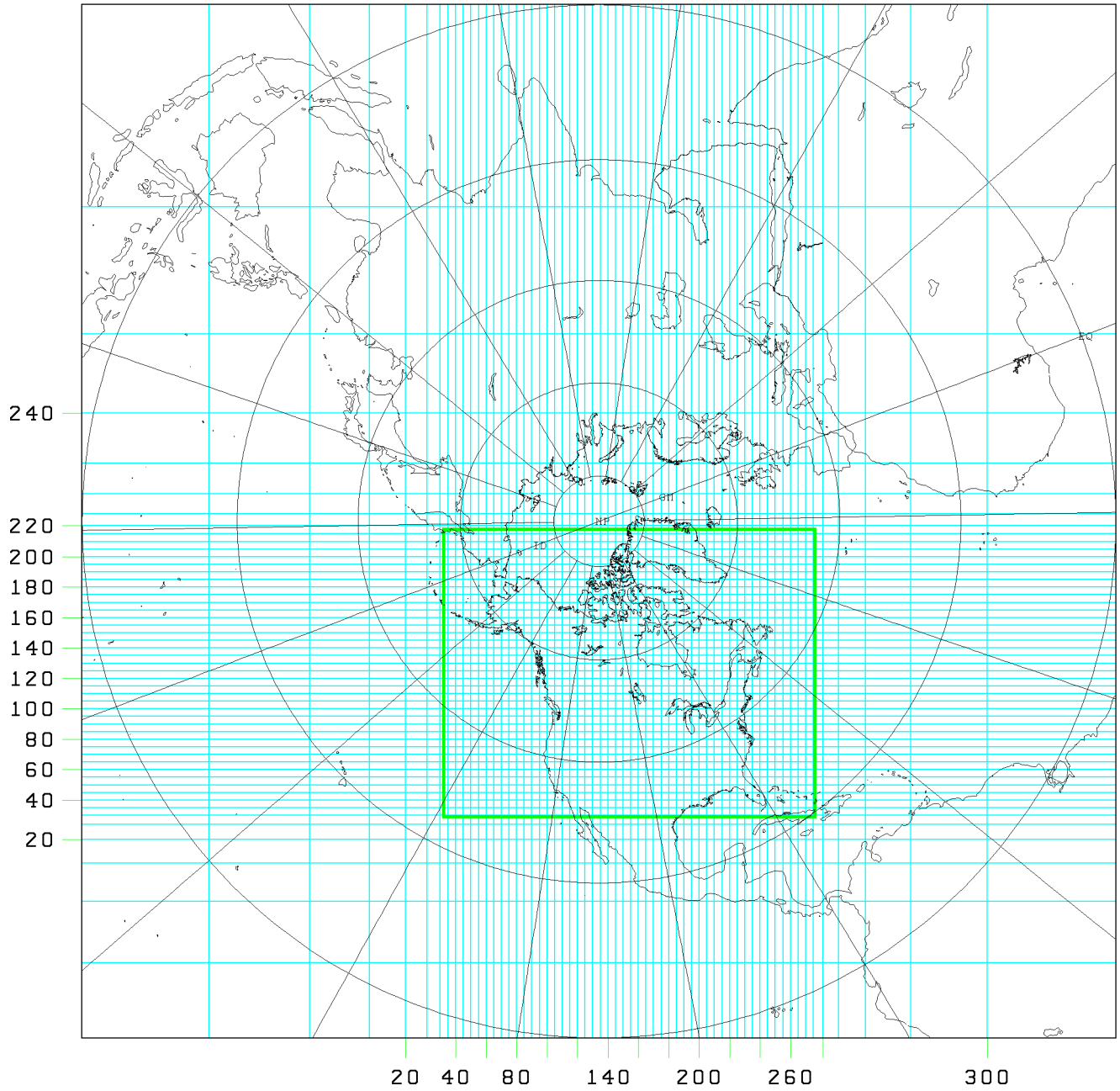
Fig. 16 Bias and r.m.s. forecast errors of the RFE and GEM models, as a function of time (going from left to right), and as measured against N. American radiosonde soundings (~ 120 per verification time). The errors for: height (dam); temperature (deg K); wind (knots); and dewpoint depression (deg K); are averaged over 118 cases from the period 01 Dec 96 - 31 Jan 97. The ordinate for each panel is pressure (hPa).

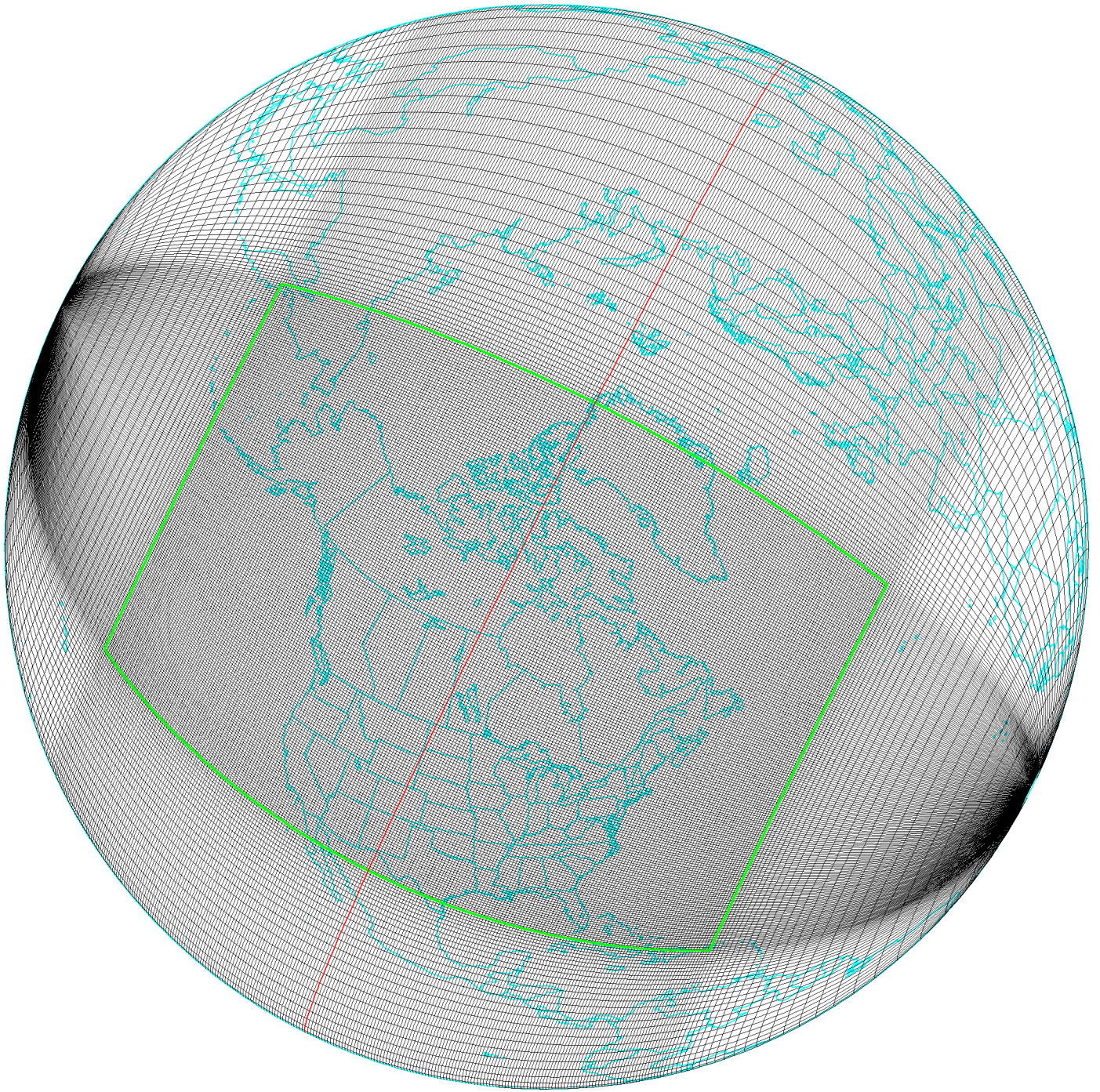
Fig. 17 Typical station distribution for the N. American radiosonde network used for the forecast verification.

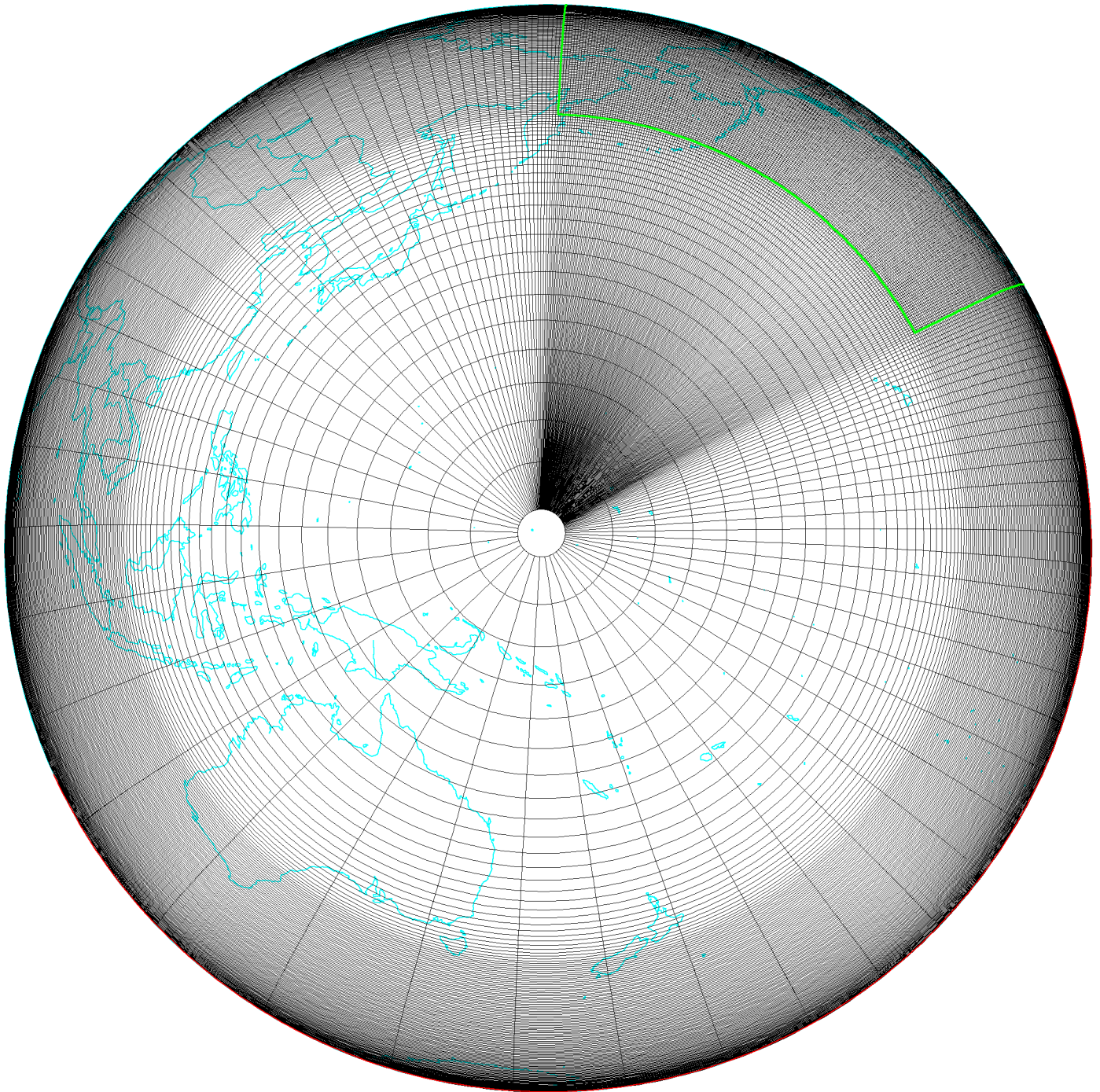
- Fig. 18** Observed (heavy) and simulated-by-GEM-model (thin) windspeeds (in knots) from 18 UTC 21 Dec 1993 to 06 UTC 22 Dec 1993 for: the downstream Grand Étang station (solid); and the upstream Sydney station (dashed).
- Fig. 19** The 200 x 300 uniform-resolution 0.02° window, centered on (63°W , 46°N), of the 329 x 418 global variable-resolution mesh used to simulate the suete.
- Fig. 20** 10-m windspeed, valid at 03 UTC 22 Dec 1993, as simulated by the GEM model after 9h of integration: contour interval: 5 knots. Wind barbs (full: 10 knots; half 5 knots) are also displayed at every 8th meshpoint in each direction. Locations of the Grand Étang and Sydney stations are respectively denoted by a thick cross and a diamond.
- Fig. 21** MSL pressure (hPa), valid at 03 UTC 22 Dec 1993, as simulated by the GEM model after 9h of integration: contour interval: 1 hPa. Locations of the Grand Étang and Sydney airport stations are respectively denoted by a thick cross and a diamond.
- Fig. 22** Bias and r.m.s. forecast errors of the SEF (dashed) and GEM (solid) models, as a function of time (going from left to right), and as measured against all available radiosonde soundings of the global network (~ 350 per verification time). The errors for: height (dam); temperature (deg K); wind (knots); and dewpoint depression (deg K); are averaged over 92 cases from the period 1 Oct - 31 Dec 1996. The ordinate for each panel is pressure (hPa).
- Fig. 23** Typical station distribution for the global radiosonde network used for the forecast verification.
- Fig. 24** Schematic for the one-dimensional variable-resolution distribution and labeling of $(N^{un} + N^{var} + 1)$ points of a domain of length $(L^{un} + L^{var})$ having a uniform-resolution sub-domain of length L^{un} , where N^{var} is restricted to be even.

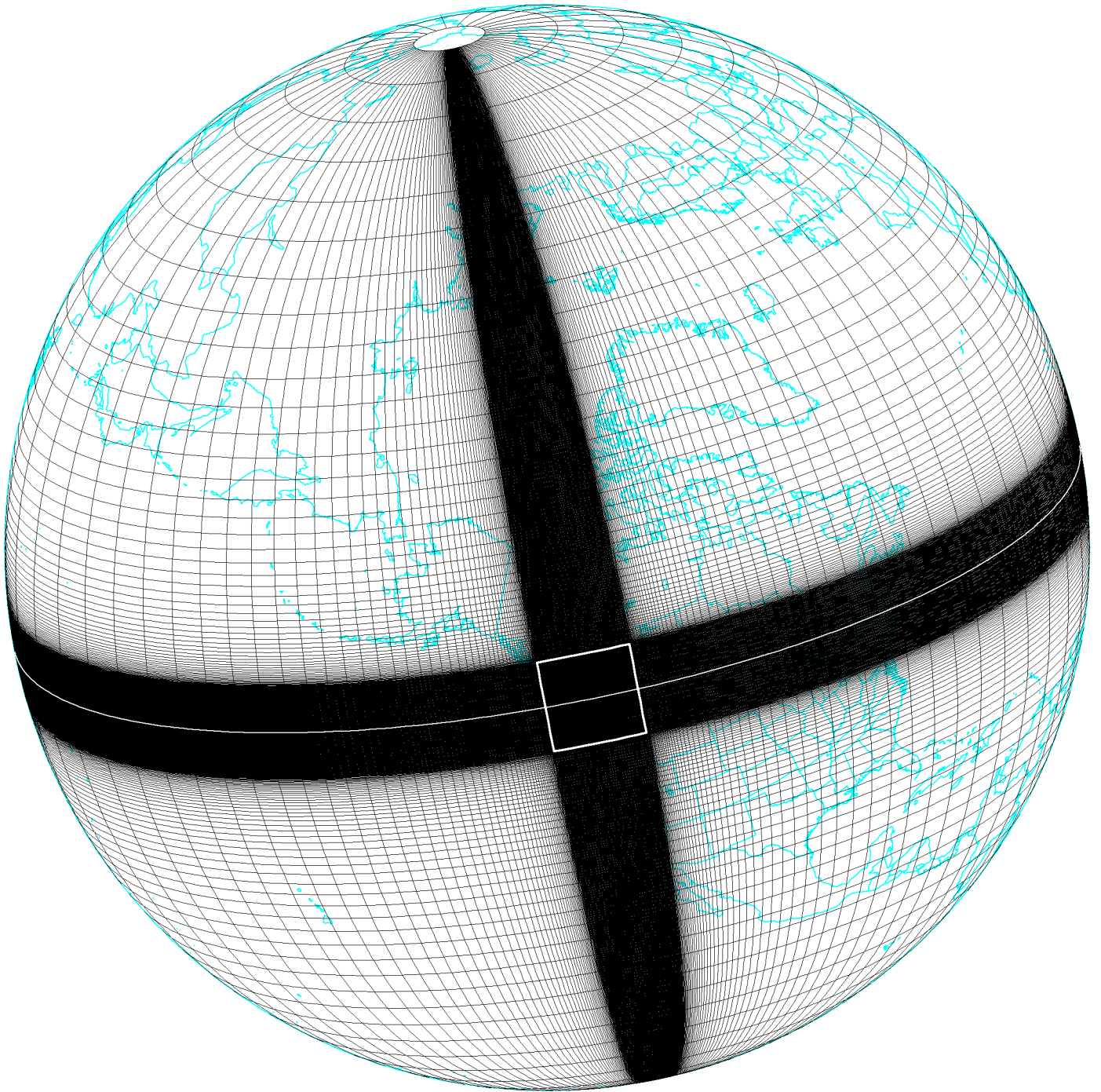
35 km

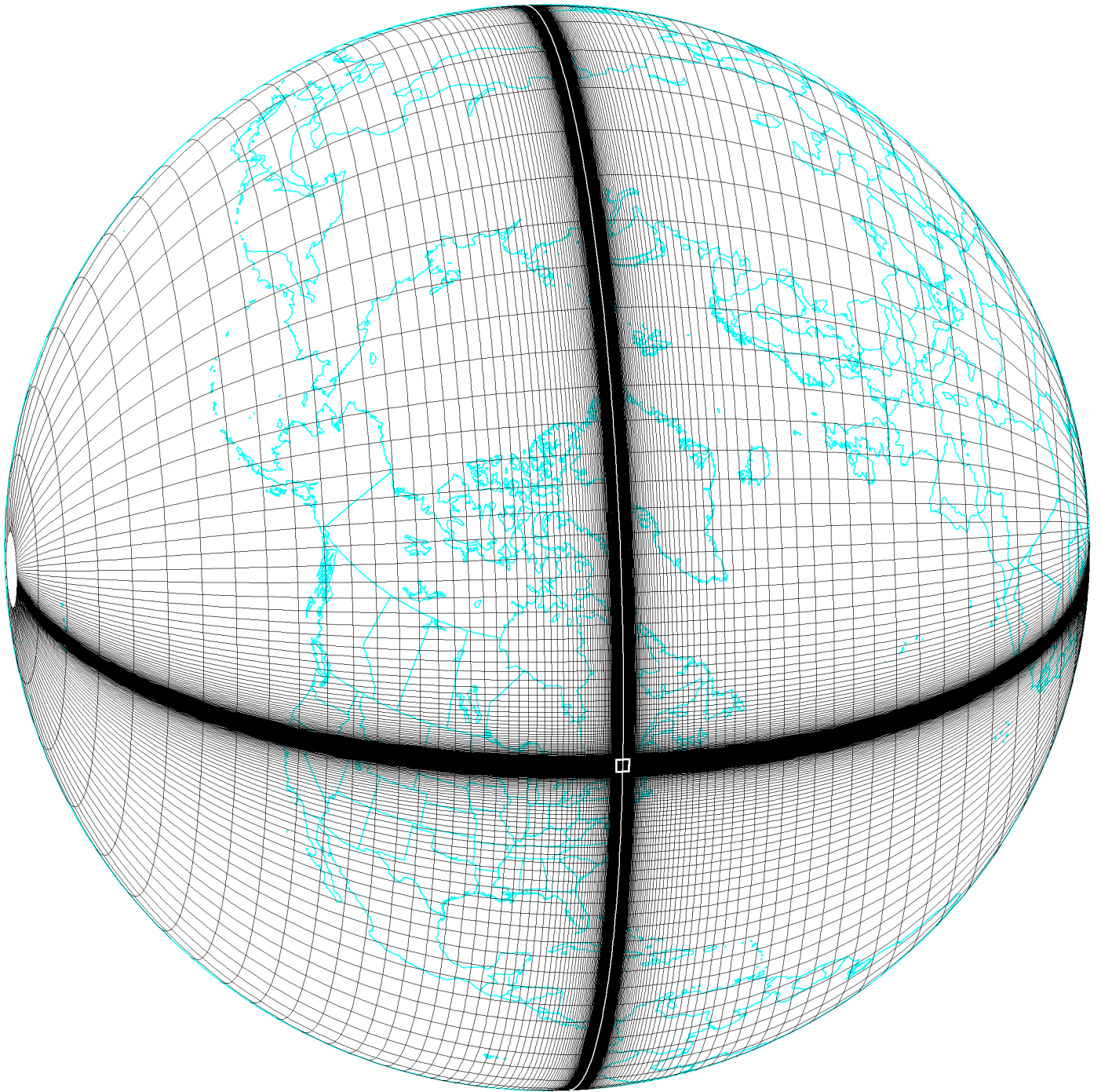
(305 x 255)

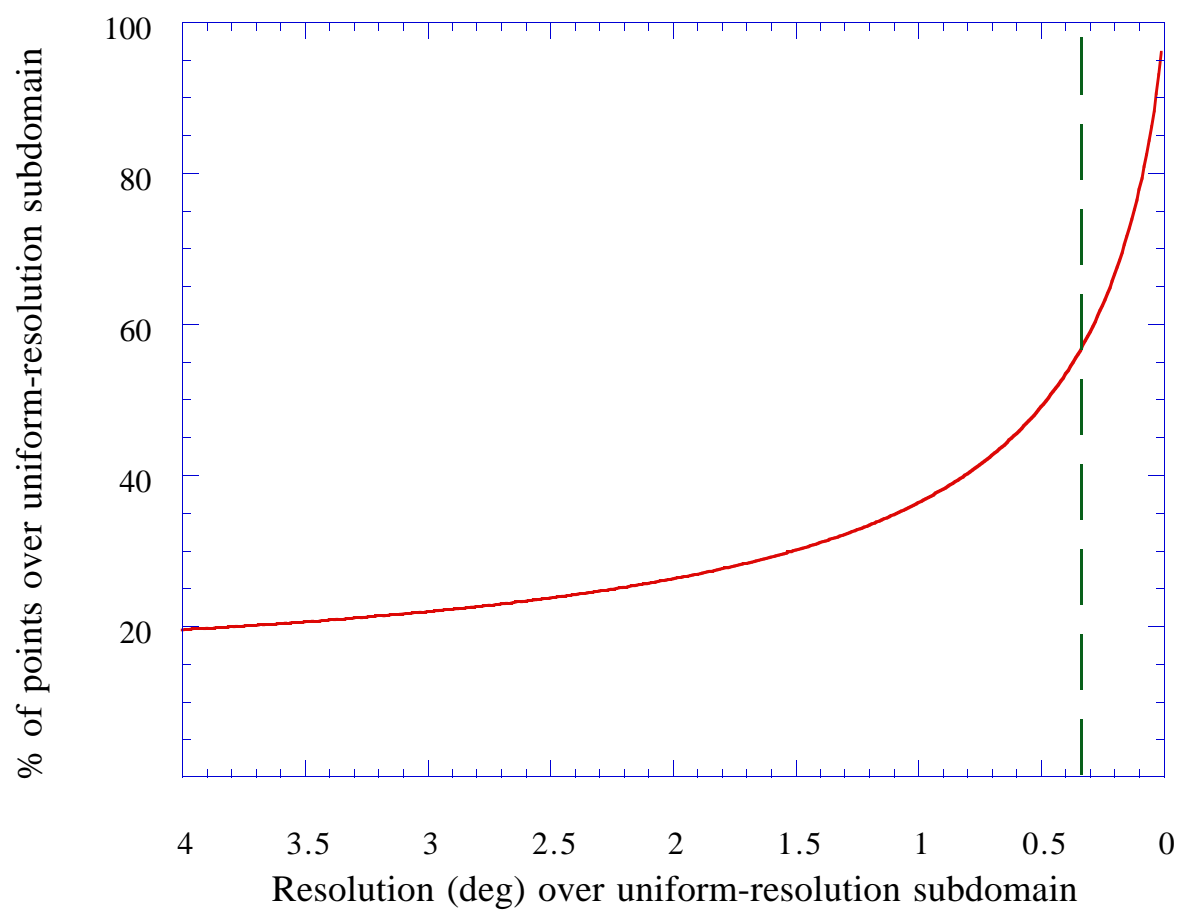


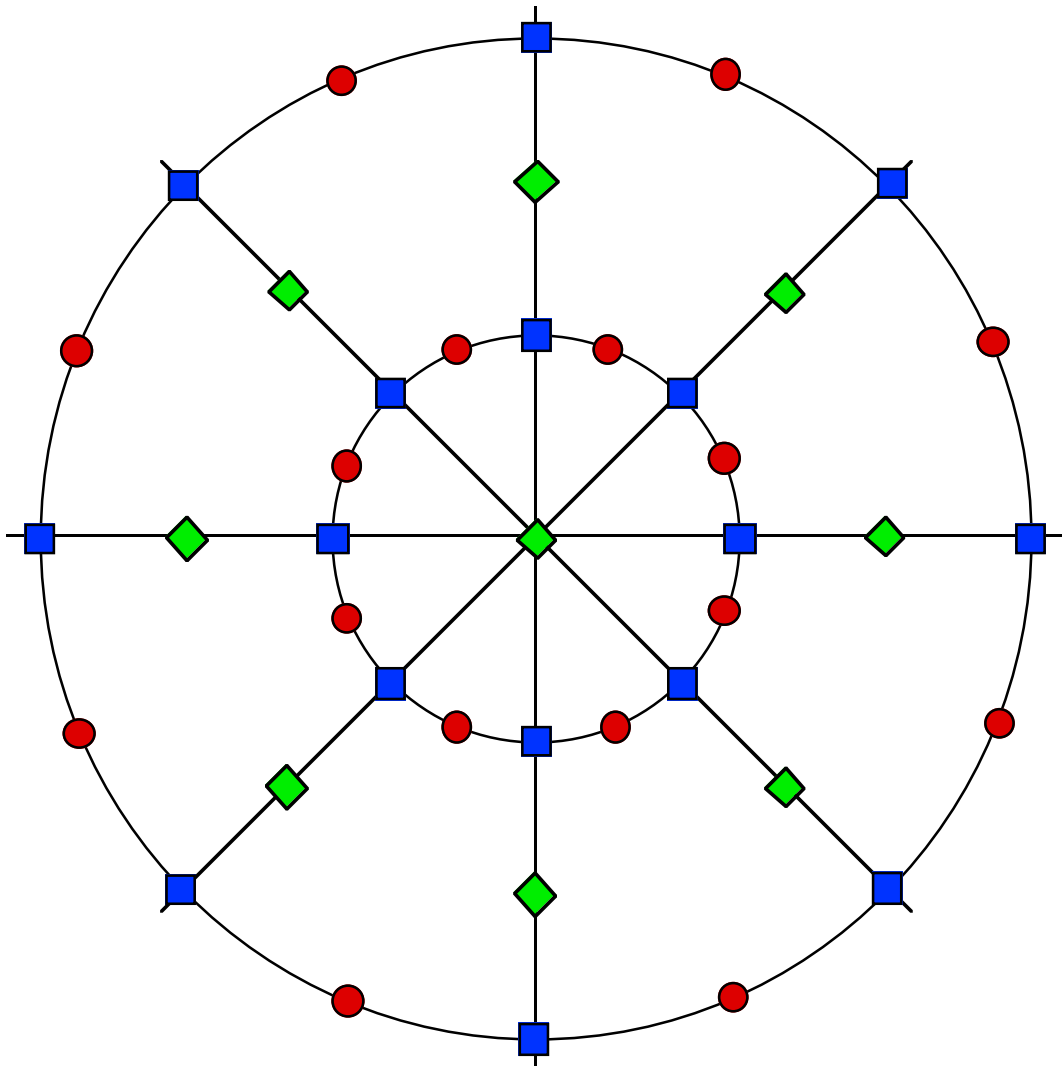


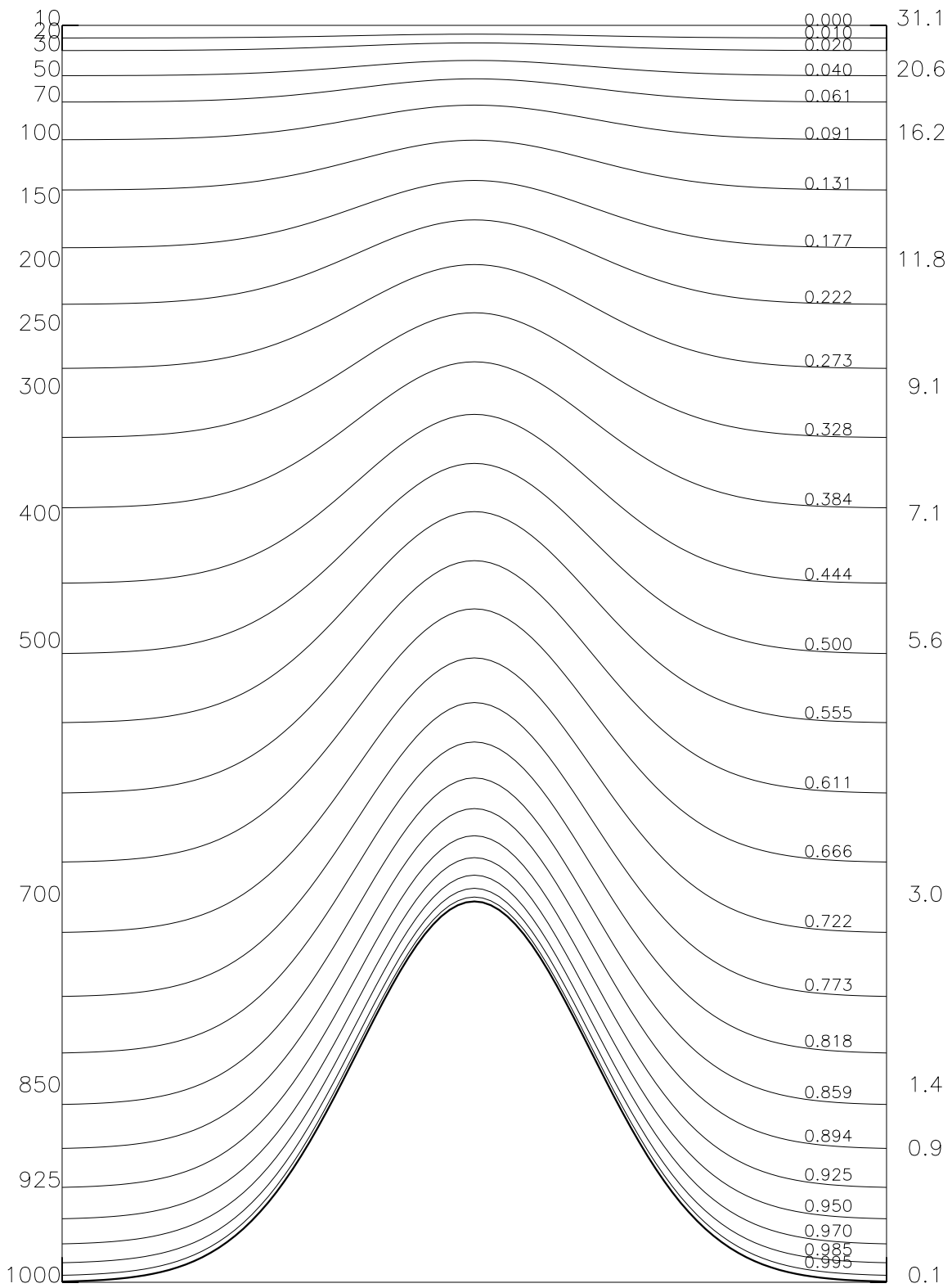






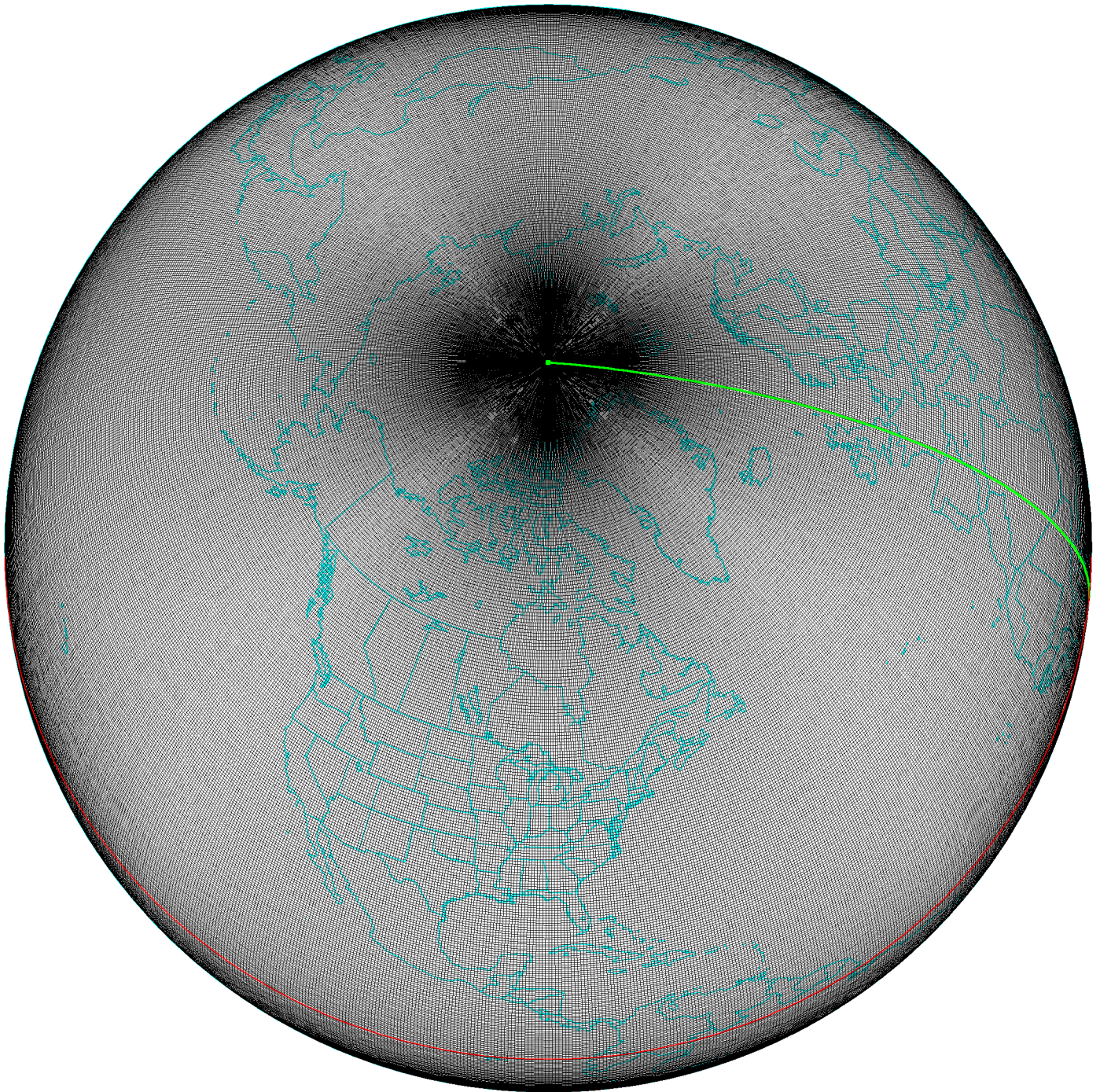


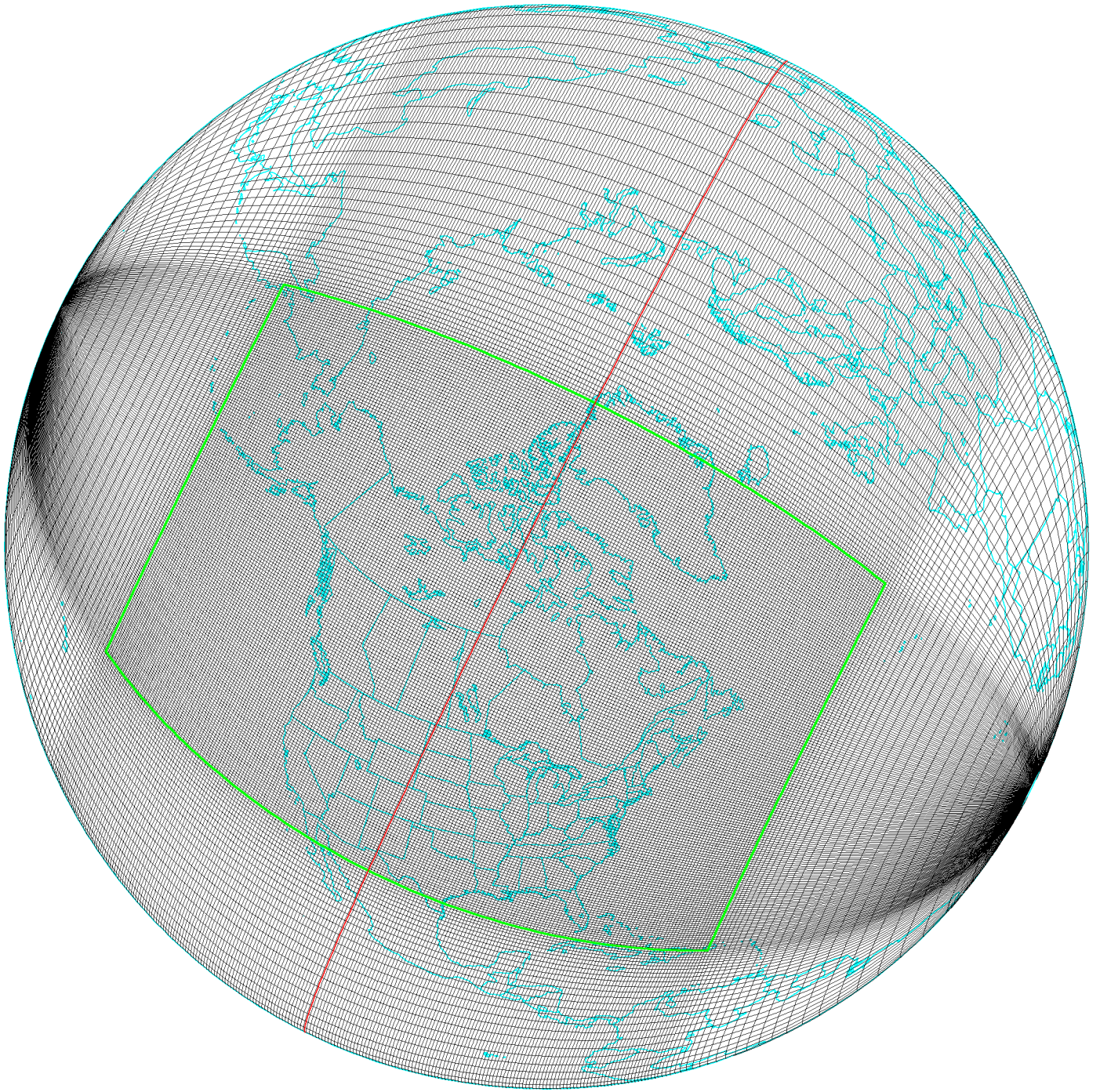


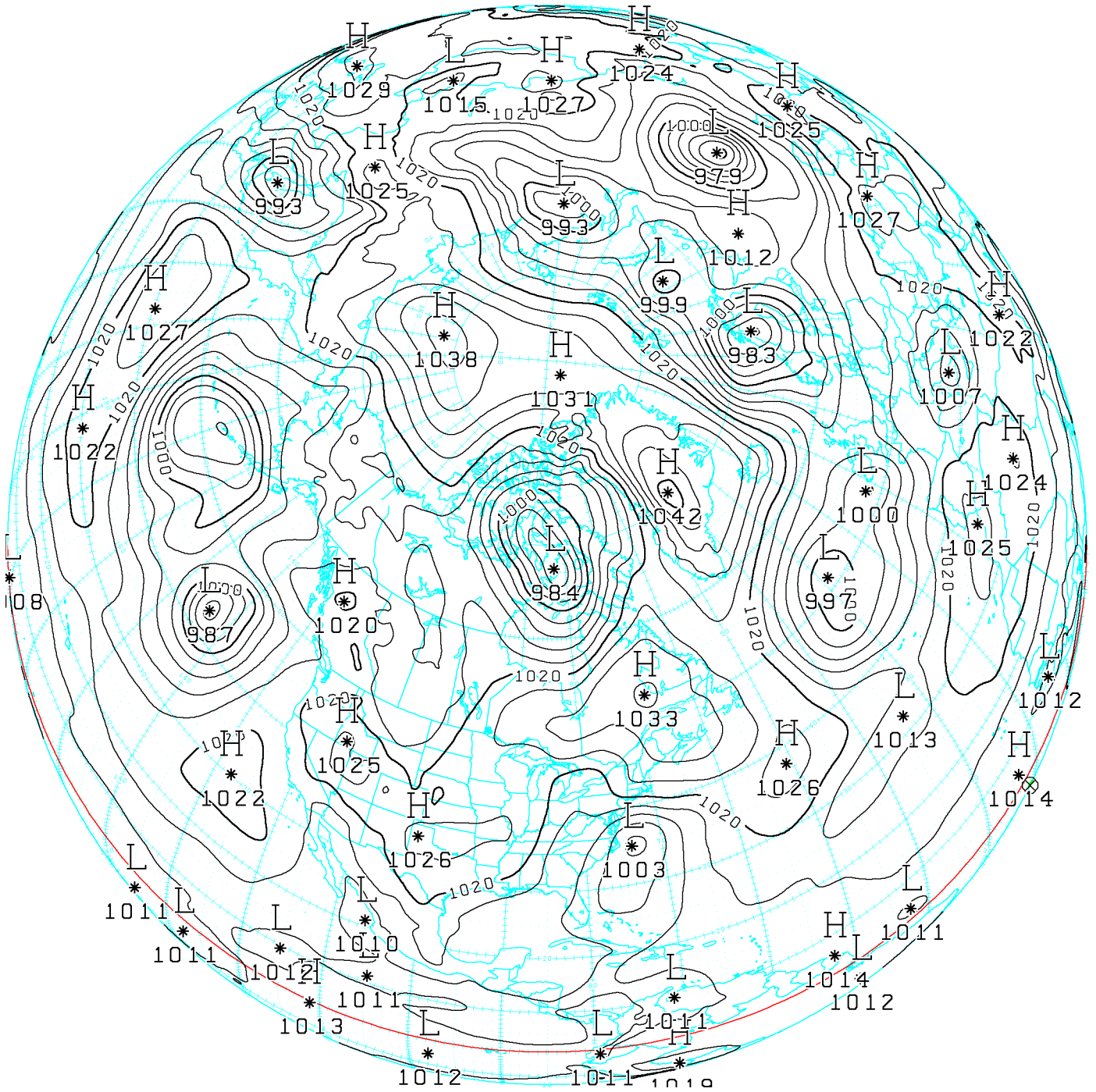


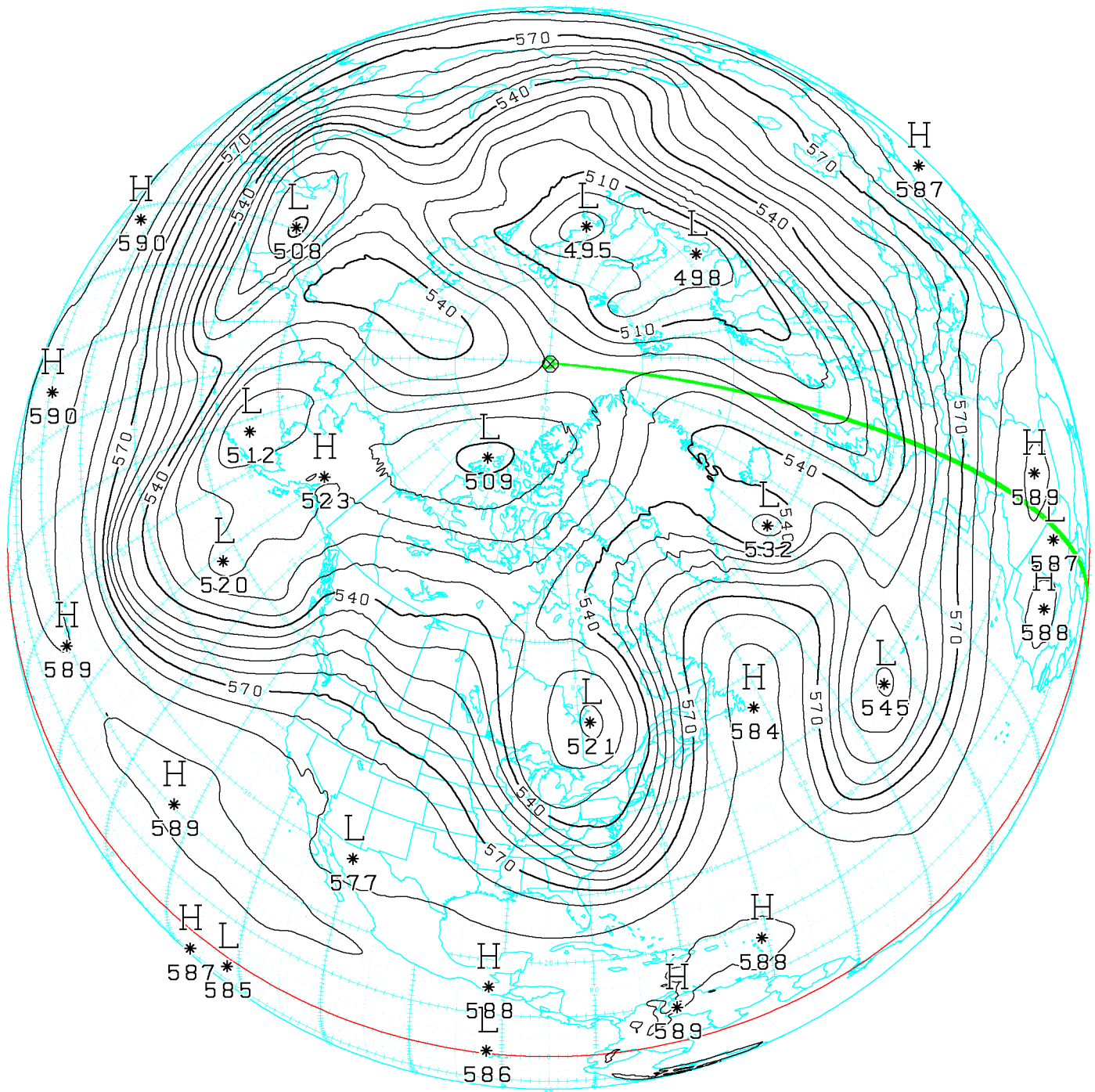
Analysis levels
(hPa)

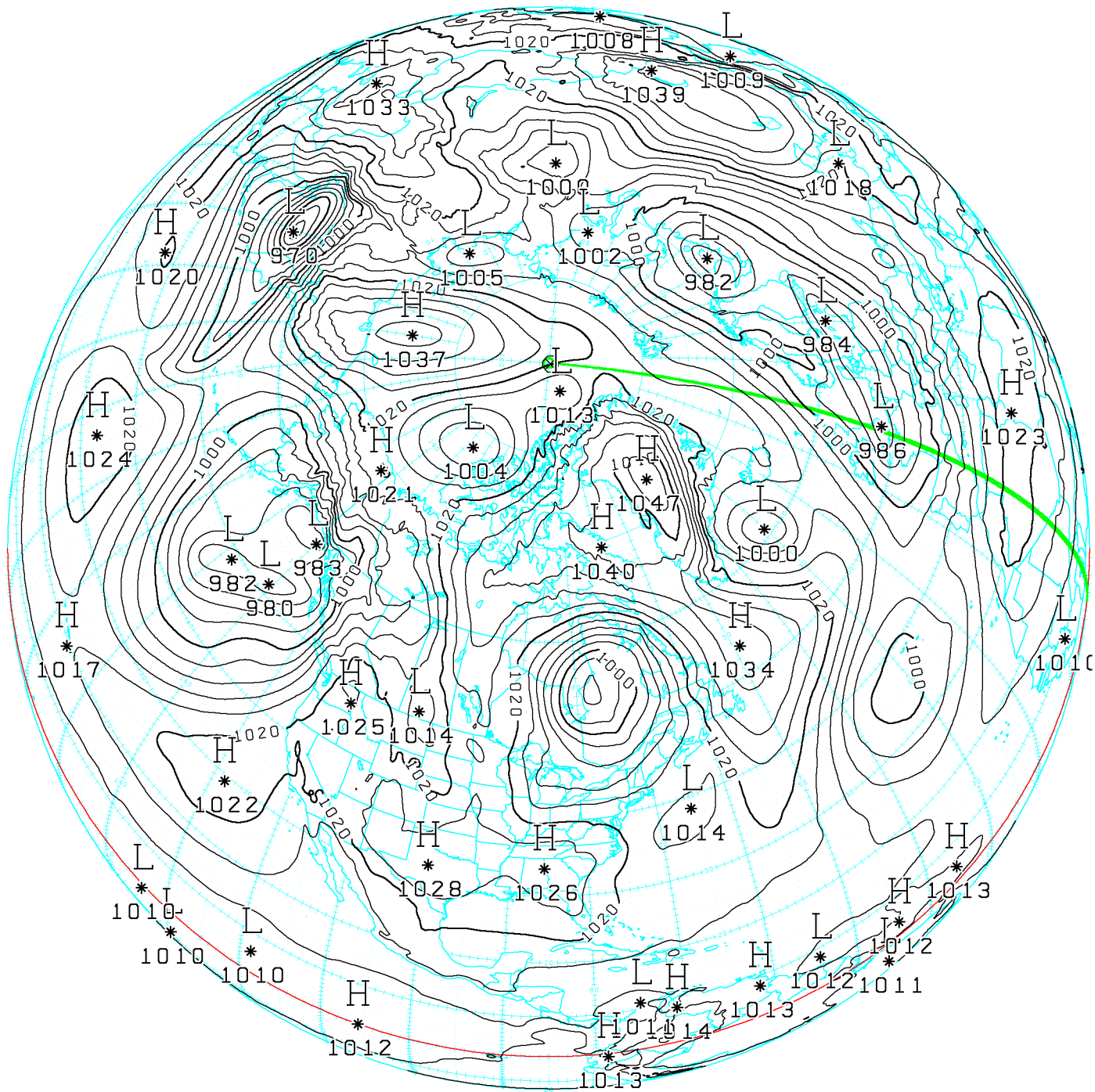
Standards heights
(Km)

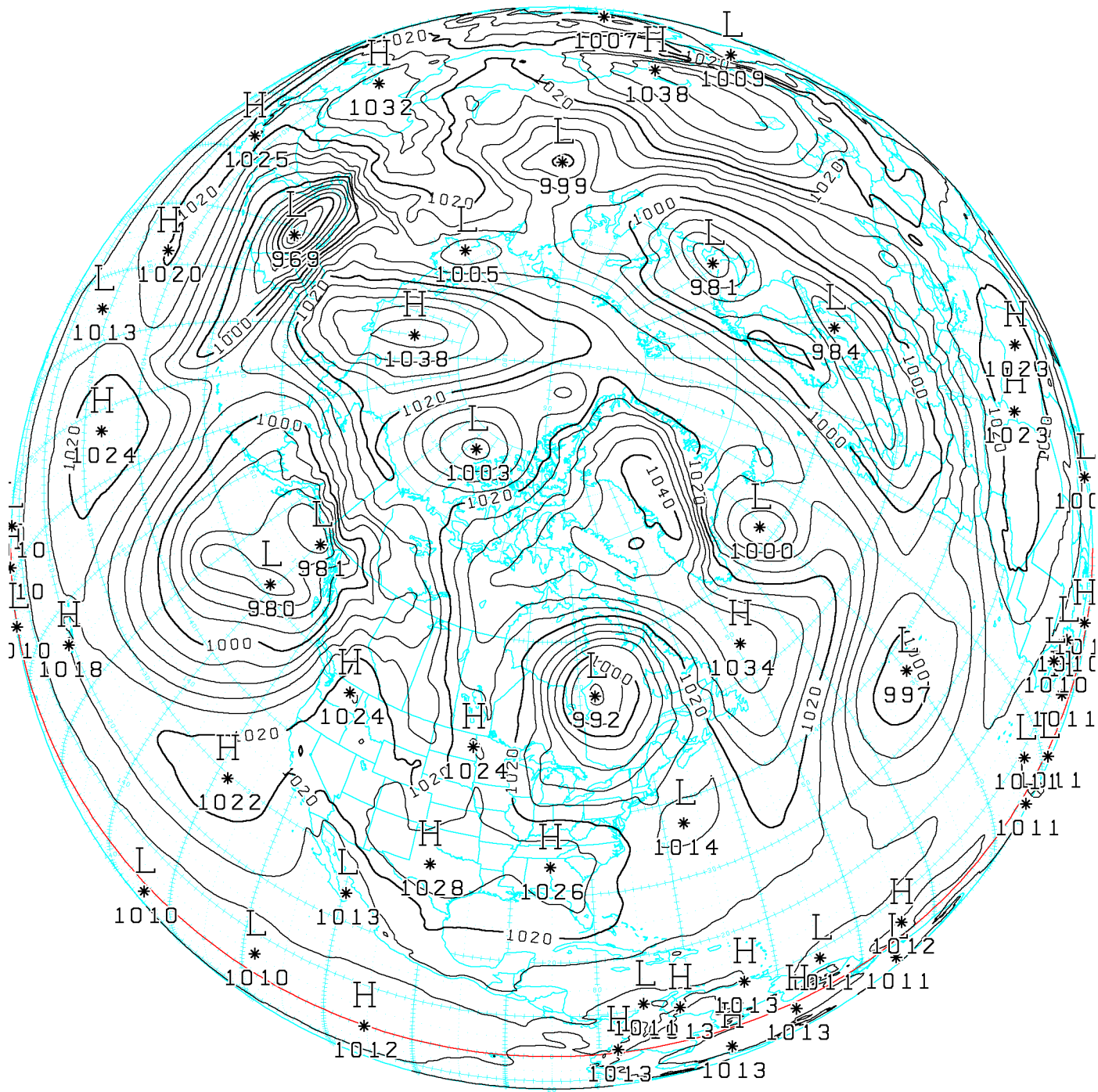


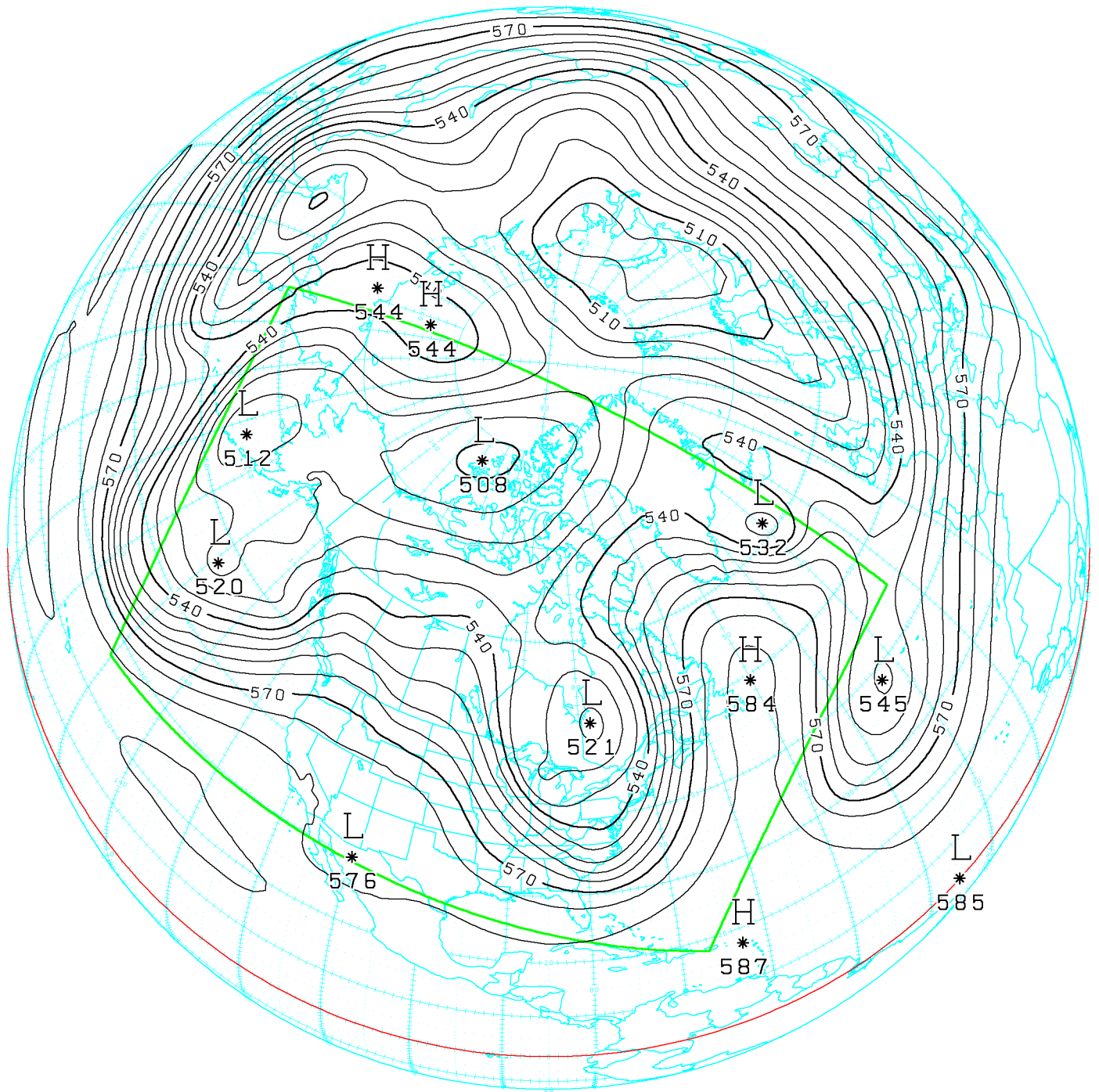


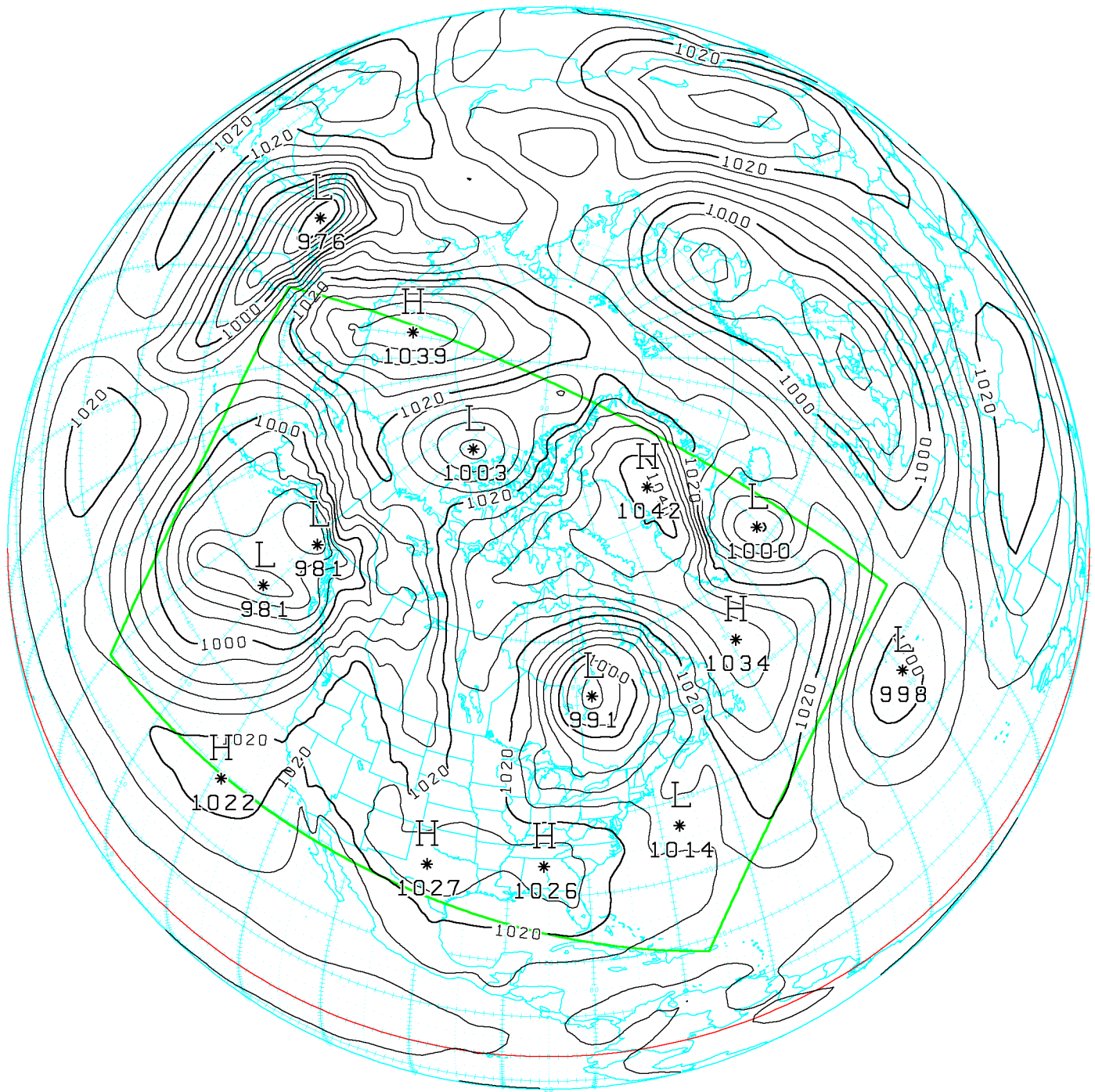


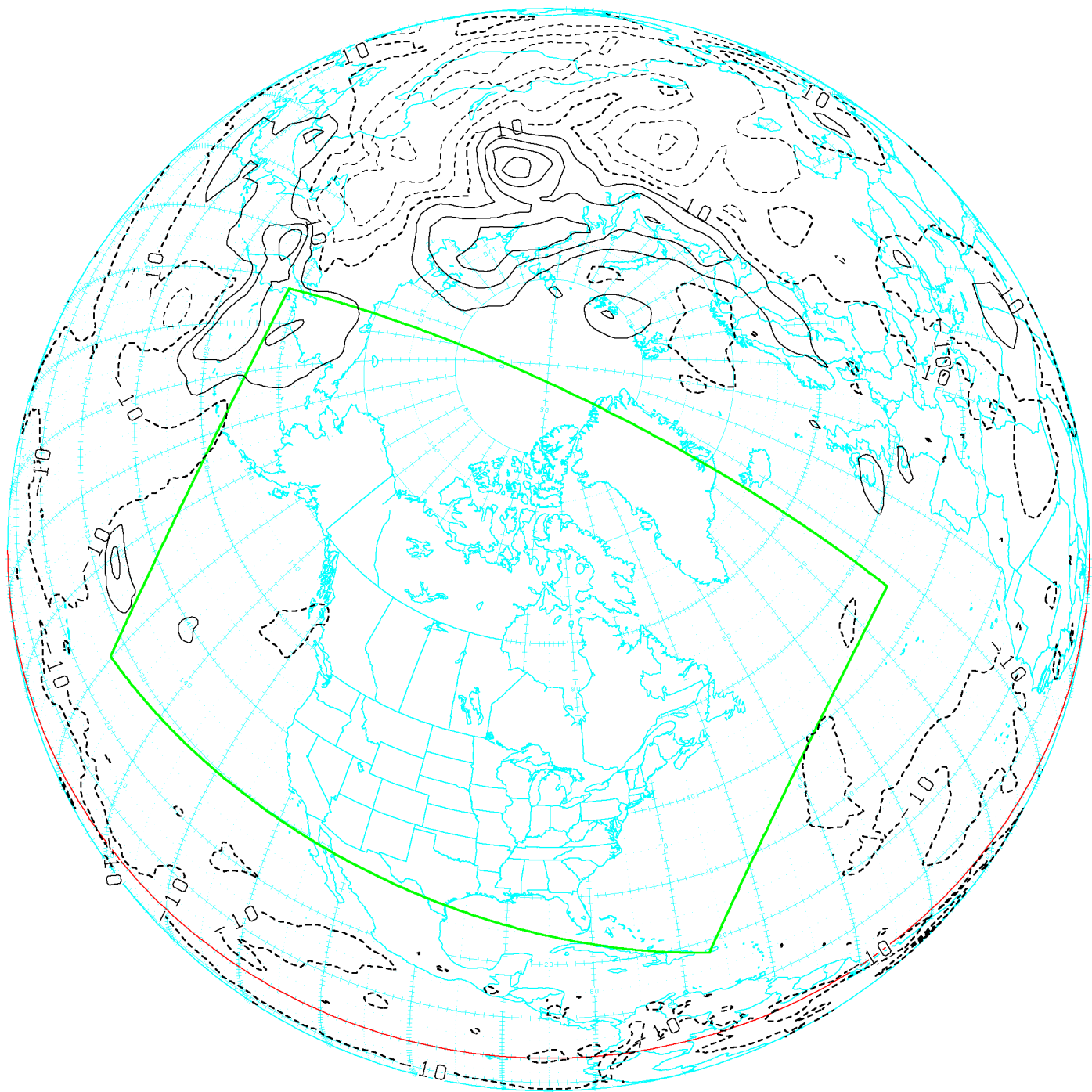




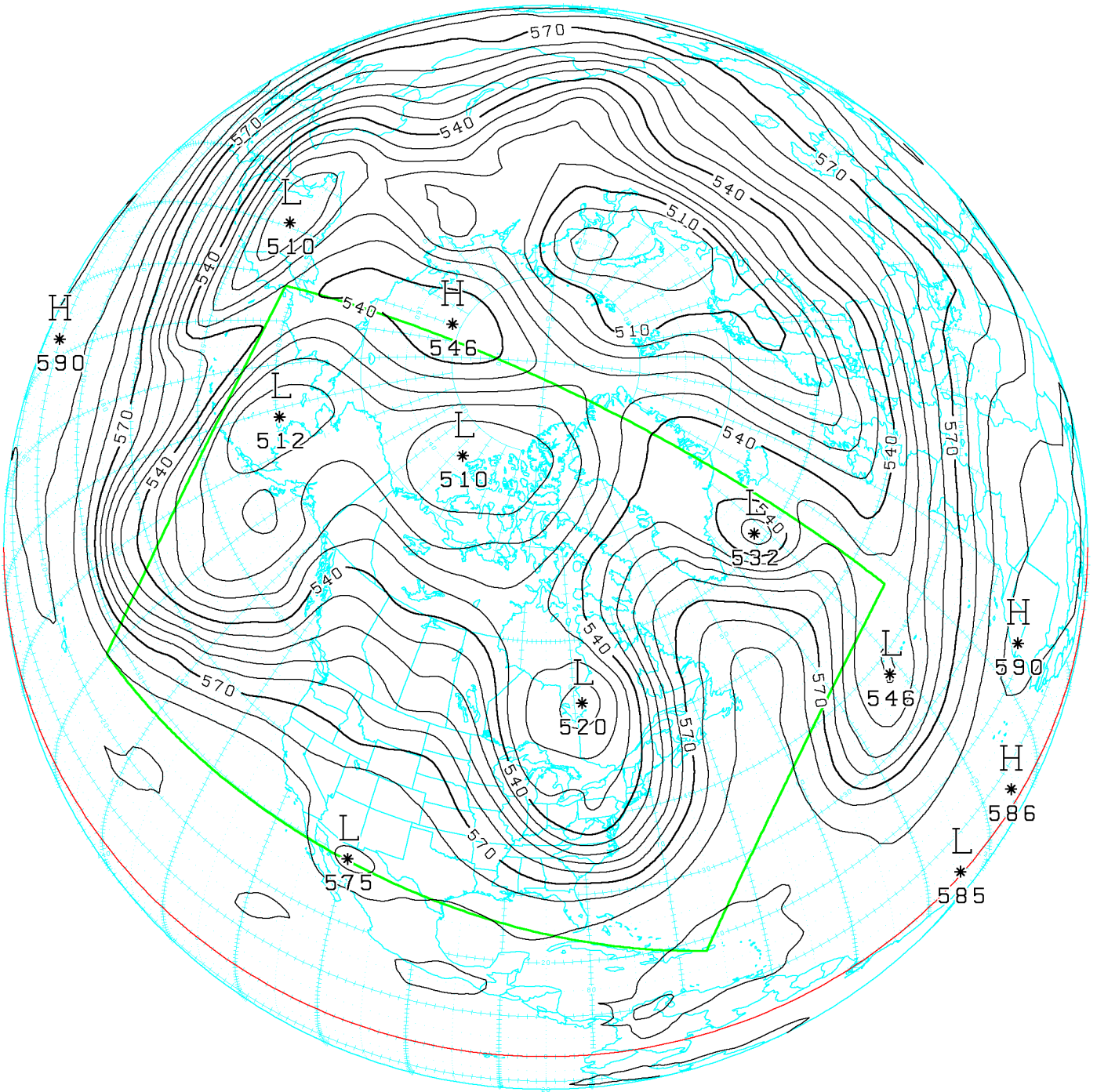


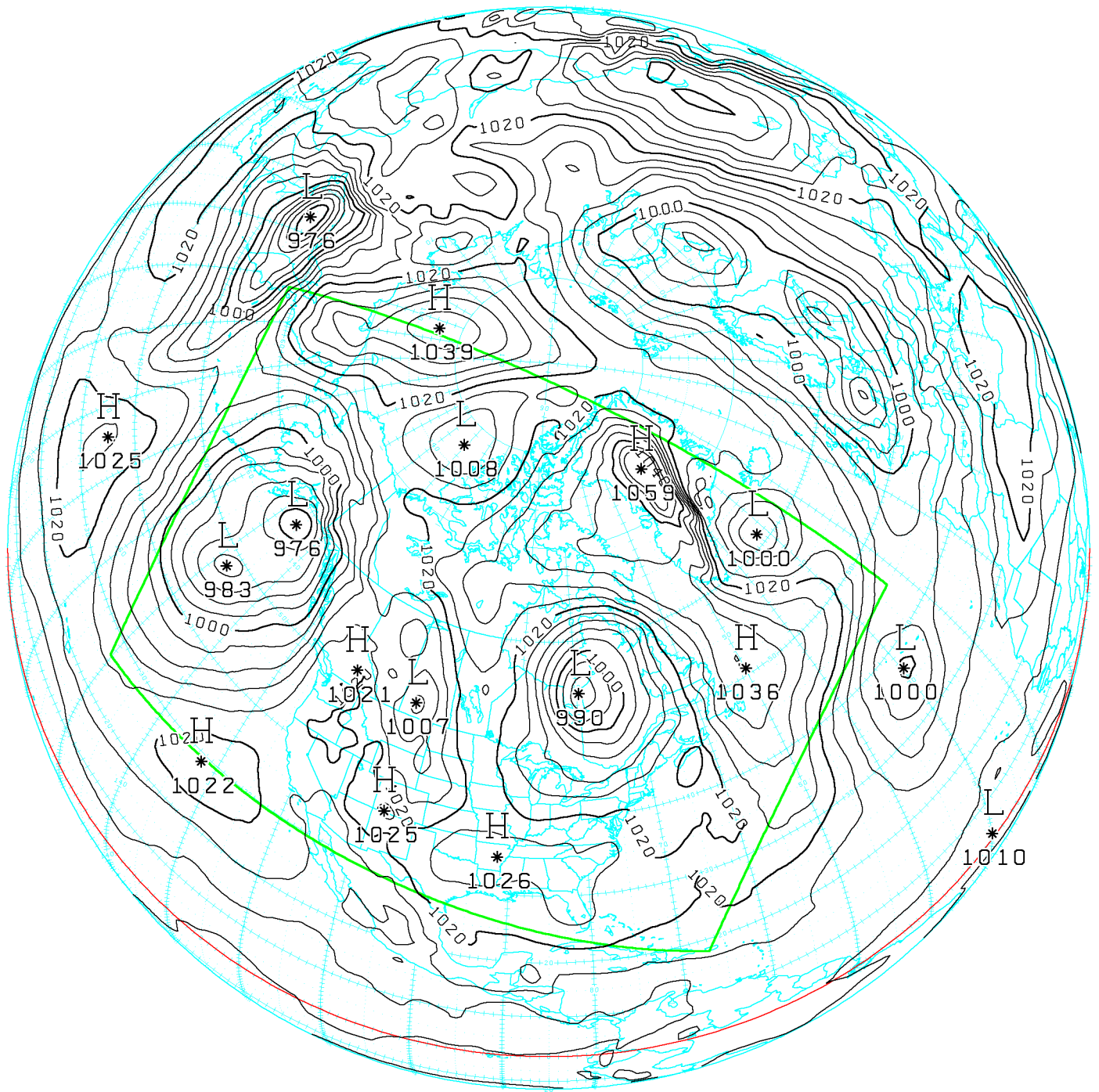


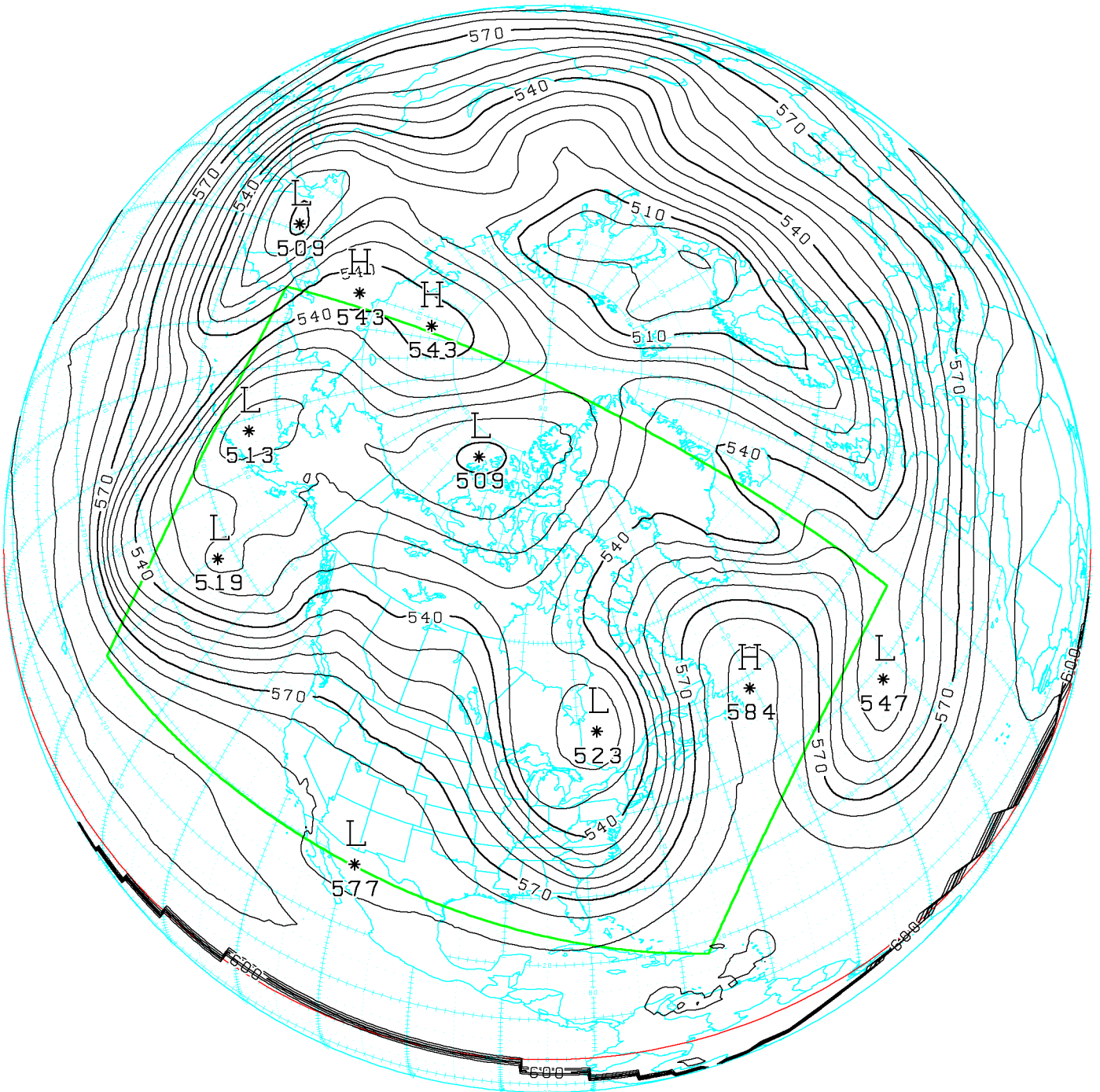


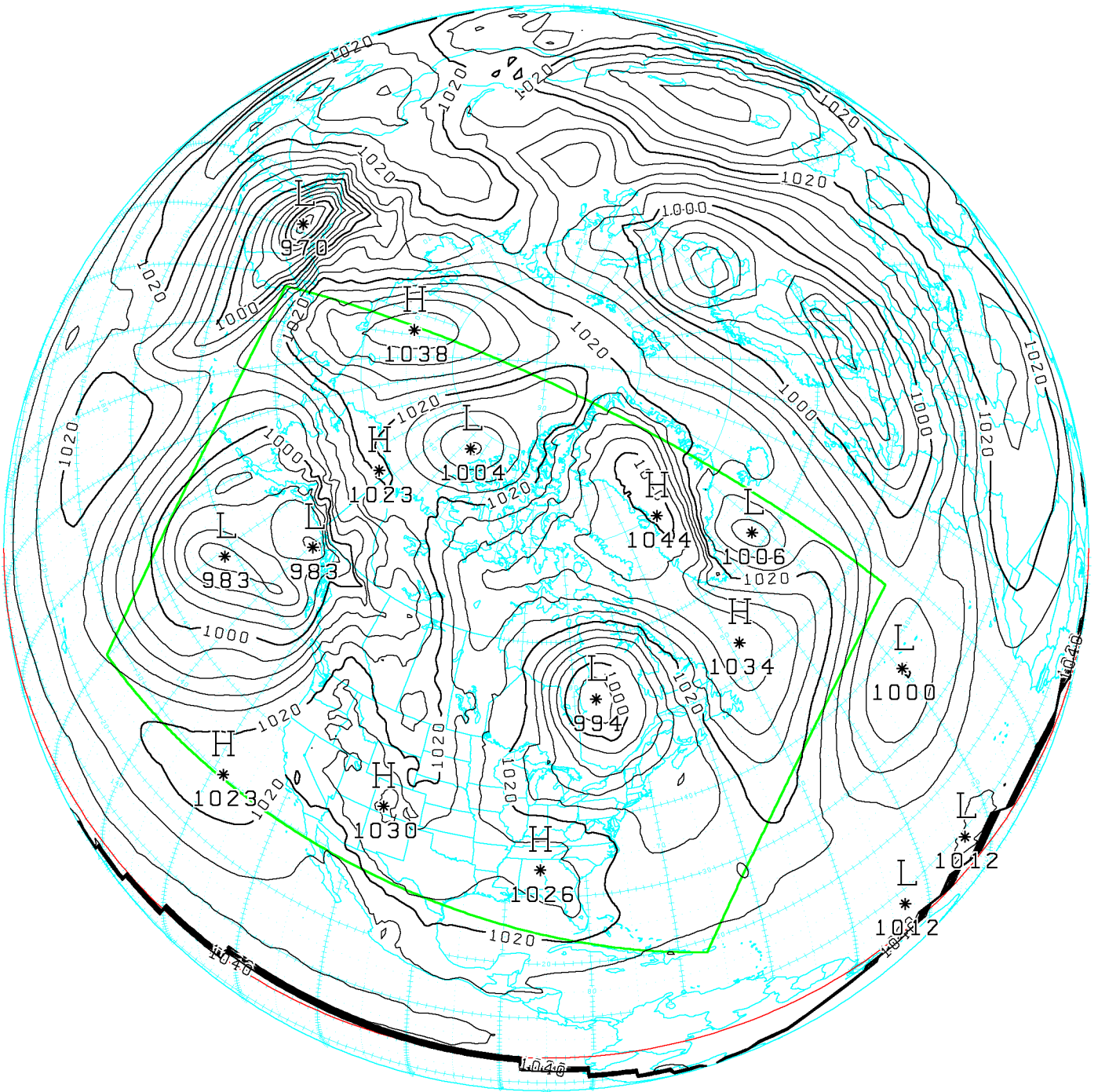












GEM (solid) vs RFE (dashed)

Bias and r.m.s. errors against N. American radiosonde soundings
Average for 118 forecasts: December 1996 and January 1997

